

# Efficient Spin-Adapted Implementation of Multireference Algebraic Diagrammatic Construction Theory. I. Core-Ionized States and X-Ray Photoelectron Spectra

Carlos E. V. de Moura\* and Alexander Yu. Sokolov\*

*Department of Chemistry and Biochemistry, The Ohio State University, Columbus, Ohio 43210, United States*

E-mail: vieirademoura.2@osu.edu; sokolov.8@osu.edu

## Abstract

We present an efficient implementation of multireference algebraic diagrammatic construction theory (MR-ADC) for simulating core-ionized states and X-ray photoelectron spectra (XPS). Taking advantage of spin adaptation, automatic code generation, and density fitting, our implementation can perform calculations for molecules with more than 1500 molecular orbitals, incorporating static and dynamic correlation in the ground and excited electronic states. We demonstrate the capabilities of MR-ADC methods by simulating the XPS spectra of substituted ferrocene complexes and azobenzene isomers. For the ground electronic states of these molecules, the XPS spectra computed using the extended second-order MR-ADC method (MR-ADC(2)-X) are in a very good agreement with available experimental results. We further show that MR-ADC can be used as a tool for interpreting or predicting the results of time-resolved XPS measurements by simulating the core ionization spectra of azobenzene along its photoisomerization, including the XPS signatures of excited states and the minimum energy conical intersection. This work is the first in a series of publications reporting the efficient implementations of MR-ADC methods.

## 1 Introduction

Understanding and harnessing light-matter interactions is a highly active area of research. Excited electronic states populated with light are central to photochemistry, solar energy conversion, and photocatalysis where light is used to enable or accelerate chemical transformations.<sup>1–12</sup> Additionally, excited states play a key role in spectroscopy where their measurements provide information about the atomic and electronic structure of chemical systems.<sup>13,14</sup> Recent advances in experimental techniques enable the spectroscopic studies of chemical systems in short-lived electronic states,<sup>15–18</sup> at non-equilibrium geometries,<sup>19,20</sup> and along reaction pathways.<sup>21–23</sup>

As spectroscopic techniques continue to evolve, there is a growing demand for quantum chemical methods that can accurately interpret or predict the spectral features of chemical systems with a wide range of nuclear geometries and elec-

tronic structures. Recently, we proposed multireference algebraic diagrammatic construction theory (MR-ADC),<sup>24,25</sup> which is a linear-response approach that allows to simulate a variety of spectroscopic properties for molecules in multiconfigurational electronic states and across potential energy surfaces. The MR-ADC methods are similar to low-order multireference perturbation theories<sup>26–34</sup> in computational cost and can compute a variety of electronic spectra (e.g., UV/Vis and X-ray absorption,<sup>35,36</sup> UV and X-ray photoelectron<sup>37–40</sup>) for chemical systems with many electrons and molecular orbitals. However, due to their inefficient spin-orbital implementation, all reported MR-ADC calculations have so far been limited to small molecules.

In this work, we demonstrate that combining spin adaptation, density fitting, and automatic code generation allows to implement MR-ADC efficiently, enabling applications to large molecules and one-electron basis sets. Focusing on the MR-

ADC methods for simulating core-ionized states and X-ray or extreme ultraviolet photoelectron spectra (XPS), this paper is the first of a series reporting fast MR-ADC implementations for a variety of spectroscopic processes. XPS is a widely used technique for the experimental characterization of molecules and materials, measuring the element-specific core-electron binding energies that are highly sensitive to oxidation states and local chemical environment.<sup>41–43</sup> The utility of XPS is further extended by the time-resolved XPS (TR-XPS) that enables studies of molecules in electronically excited states and along the course of chemical reactions.<sup>44–56</sup> However, the XPS and TR-XPS spectra usually exhibit broad overlapping features that can be difficult to interpret without insights from accurate theoretical calculations.

Here, we demonstrate the capabilities of our efficient MR-ADC implementation by simulating and interpreting the XPS spectra of substituted ferrocene complexes in their ground electronic states and the azobenzene molecule along its excited-state isomerization. Our calculations employ large core-valence polarized basis sets correlating all electrons in up to 1532 molecular orbitals. For the substituted ferrocene complexes, we show that the carbon K-edge XPS spectra simulated using the extended second-order MR-ADC method (MR-ADC(2)-X) are in a very good agreement with the experimental data, providing accurate interpretation of overlapping spectral features. In our study of azobenzene, we predict the carbon and nitrogen K-edge XPS signatures of ground and excited electronic states at the *cis*, *trans*, and conical intersection geometries, which may be helpful in interpreting the results of TR-XPS experiments in the future.

Our paper is organized as follows. First, we briefly cover the theoretical foundations of MR-ADC for simulating core-ionized states and XPS spectra and discuss its spin adaptation (Section 2). We then describe the details of our efficient implementation, including the automatic generation of spin-adapted code and density fitting (Section 3). We provide the computational details in Section 4 and present the applications of MR-ADC methods to substituted ferrocene complexes and azobenzene photoisomerization in Section 5. Our conclusions are presented in Section 6. Additional computational details and working equations are provided in the Supplementary Information.

## 2 Theory

### 2.1 Multireference algebraic diagrammatic construction theory

Multireference algebraic diagrammatic construction (MR-ADC) simulates electronic excitations and spectra by approximating a retarded propagator (also known as a linear-response function) using multireference perturbation theory.<sup>25,57</sup> A retarded propagator describes the response of a chemical system in an electronic state  $|\Psi\rangle$  with energy  $E$  to a periodic perturbation with frequency  $\omega$  and has a general form:

$$\begin{aligned} G_{\mu\nu}(\omega) &= G_{\mu\nu}^+(\omega) \pm G_{\mu\nu}^-(\omega) \\ &= \langle \Psi | q_\mu (\omega - H + E)^{-1} q_\nu^\dagger | \Psi \rangle \\ &\quad \pm \langle \Psi | q_\nu^\dagger (\omega + H - E)^{-1} q_\mu | \Psi \rangle, \end{aligned} \quad (1)$$

where  $G_{\mu\nu}^+$  and  $G_{\mu\nu}^-$  are called the forward and backward components and  $H$  is the electronic (Born–Oppenheimer) Hamiltonian. The operators  $q_\mu$  and  $q_\nu^\dagger$  define the nature of periodic perturbation (e.g., electric or magnetic field), the physical observables of interest (e.g., density of states, polarization), and the sign of the second term.

Depending on the form of operators  $q_\mu$  and  $q_\nu^\dagger$ , MR-ADC can simulate a variety of spectroscopic processes, including electronic excitations in UV/Vis absorption spectroscopy,<sup>24,35</sup> ionization and electron attachment in photoelectron experiments,<sup>37,38</sup> and core excitations in X-ray absorption or photoelectron measurements.<sup>36,39,40</sup> Similar to its single-reference counterpart,<sup>57–63</sup> MR-ADC expresses Eq. (1) in a mathematical form where  $G_{\mu\nu}^+$  and  $G_{\mu\nu}^-$  are independently represented in terms of non-diagonal tensors

$$\mathbf{G}_\pm(\omega) = \mathbf{T}_\pm(\omega \mathbf{S}_\pm - \mathbf{M}_\pm)^{-1} \mathbf{T}_\pm^\dagger, \quad (2)$$

which are called the effective Hamiltonian ( $\mathbf{M}_\pm$ ), effective transition moments ( $\mathbf{T}_\pm$ ), and overlap ( $\mathbf{S}_\pm$ ) matrices. Here,  $\mathbf{M}_\pm$  and  $\mathbf{T}_\pm$  are expressed in a basis of nonorthogonal excitations with overlap  $\mathbf{S}_\pm$  and contain information about the energies and probabilities of electronic transitions for a specific spectroscopic process, respectively.

Expanding  $\mathbf{M}_\pm$ ,  $\mathbf{T}_\pm$ , and  $\mathbf{S}_\pm$  using multireference

perturbation theory

$$\mathbf{M}_{\pm} \approx \mathbf{M}_{\pm}^{(0)} + \mathbf{M}_{\pm}^{(1)} + \dots + \mathbf{M}_{\pm}^{(n)}, \quad (3)$$

$$\mathbf{T}_{\pm} \approx \mathbf{T}_{\pm}^{(0)} + \mathbf{T}_{\pm}^{(1)} + \dots + \mathbf{T}_{\pm}^{(n)}, \quad (4)$$

$$\mathbf{S}_{\pm} \approx \mathbf{S}_{\pm}^{(0)} + \mathbf{S}_{\pm}^{(1)} + \dots + \mathbf{S}_{\pm}^{(n)}, \quad (5)$$

and truncating these expansions at order ( $n$ ) defines the hierarchy of MR-ADC( $n$ ) approximations. To ensure that the MR-ADC( $n$ ) methods are free from intruder-state problems,<sup>64–66</sup> the series in Eqs. (3) to (5) are generated with respect to the reference complete active space self-consistent field (CASSCF) wavefunction ( $|\Psi_0\rangle$ ) and the perturbation operator  $V = H - H^{(0)}$ , where  $H^{(0)}$  is the Dyall zeroth-order Hamiltonian.<sup>25,67</sup>

The MR-ADC( $n$ ) excitation energies relative to the reference state are computed as the eigenvalues of  $\mathbf{M}_{\pm}$  ( $\mathbf{\Omega}_{\pm}$ ) by solving the Hermitian generalized eigenvalue problem

$$\mathbf{M}_{\pm} \mathbf{Y}_{\pm} = \mathbf{S}_{\pm} \mathbf{Y}_{\pm} \mathbf{\Omega}_{\pm}. \quad (6)$$

The eigenvectors  $\mathbf{Y}_{\pm}$  are used to compute the spectroscopic amplitudes

$$\mathbf{X}_{\pm} = \mathbf{T}_{\pm} \mathbf{S}_{\pm}^{-1/2} \mathbf{Y}_{\pm} \quad (7)$$

that provide access to transition intensities, densities of states, and spectra. When expressed in the eigenstate basis of  $\mathbf{M}_{\pm}$ , the MR-ADC( $n$ ) propagator can be written as

$$\mathbf{G}_{\pm}(\omega) = \mathbf{X}_{\pm}(\omega \mathbf{1} - \mathbf{\Omega}_{\pm})^{-1} \mathbf{X}_{\pm}^{\dagger}, \quad (8)$$

which is known as its spectral representation.

## 2.2 MR-ADC for core-ionized states and X-ray photoelectron spectra

In this work, we will focus on the MR-ADC methods for simulating core-ionized states and X-ray photoelectron spectra, which are derived from the backward component of one-particle Green’s function<sup>68,69</sup>

$$G_{-pq}(\omega) = \langle \Psi | a_q^{\dagger}(\omega + H - E)^{-1} a_p | \Psi \rangle. \quad (9)$$

Approximating  $\mathbf{G}_{-}(\omega)$  in Eq. (9) following the approach described in Section 2.1 gives rise to the MR-ADC( $n$ ) approximations that describe the ( $N - 1$ )-electron ionized states starting from the  $N$ -electron CASSCF wavefunction (IP-MR-ADC).<sup>37,38</sup> In contrast to conventional multirefer-

ence perturbation theories for excited states,<sup>26–34</sup> the IP-MR-ADC methods do not require separate calculations for the reference and ionized states, and can simulate excitations in all (active and non-active) molecular orbitals. These features make IP-MR-ADC particularly attractive for calculating the excited states and spectra measured in X-ray photoelectron spectroscopy (XPS) experiments where an electron is ejected from a core or inner-shell valence orbital following the excitation with X-ray or extreme ultraviolet light. However, computing these high-energy states directly by solving the generalized eigenvalue problem in Eq. (6) is very difficult as they are deeply embedded in the eigenstate spectrum of IP-MR-ADC effective Hamiltonian matrix  $\mathbf{M}_{-}$ .

To overcome this challenge, IP-MR-ADC is combined with a core-valence separation (CVS)<sup>70–74</sup> approximation that neglects the coupling between valence- and core-ionized states due to their large difference in energy and spatial localization.<sup>39,40</sup> In the CVS-IP-MR-ADC methods, the molecular orbitals of the system are split into four subsets: “core”, “valence”, “active”, and “virtual” (Figure 1). The union of core and valence subspaces corresponds to the doubly occupied non-active orbitals in the reference CASSCF wavefunction  $|\Psi_0\rangle$ . The core subspace includes all lowest-energy molecular orbitals starting with the one that is expected to be ionized first in the XPS spectrum. The remaining non-active occupied orbitals are incorporated in the valence subspace. The CVS-IP-MR-ADC matrices ( $\mathbf{M}_{-}$ ,  $\mathbf{T}_{-}$ , and  $\mathbf{S}_{-}$ ) are expressed in the basis of ionized electronic configurations  $|\Psi_{\mu}^{(k)}\rangle = h_{-\mu}^{(k)\dagger} |\Psi_0\rangle$  where the  $k$ th-order excitation operators  $h_{-\mu}^{(k)\dagger}$  are required to ionize or excite an electron from at least one core orbital (Figure 1).

The  $n$ th-order contributions to  $\mathbf{M}_{-}$ ,  $\mathbf{T}_{-}$ , and  $\mathbf{S}_{-}$  have the form:

$$M_{-\mu\nu}^{(n)} = \sum_{klm}^{k+l+m=n} \langle \Psi_0 | [h_{-\mu}^{(k)\dagger}, [\tilde{H}^{(l)}, h_{-\nu}^{(m)}]]_{+} | \Psi_0 \rangle, \quad (10)$$

$$T_{-p\nu}^{(n)} = \sum_{kl}^{k+l=n} \langle \Psi_0 | [\tilde{a}_p^{(k)}, h_{-\nu}^{(l)}]_{+} | \Psi_0 \rangle, \quad (11)$$

$$S_{-\mu\nu}^{(n)} = \sum_{kl}^{k+l=n} \langle \Psi_0 | [h_{-\mu}^{(k)\dagger}, h_{-\nu}^{(l)}]_{+} | \Psi_0 \rangle, \quad (12)$$

where  $\tilde{H}^{(k)}$  and  $\tilde{a}_p^{(k)}$  are the  $k$ th-order components of effective Hamiltonian and effective observable

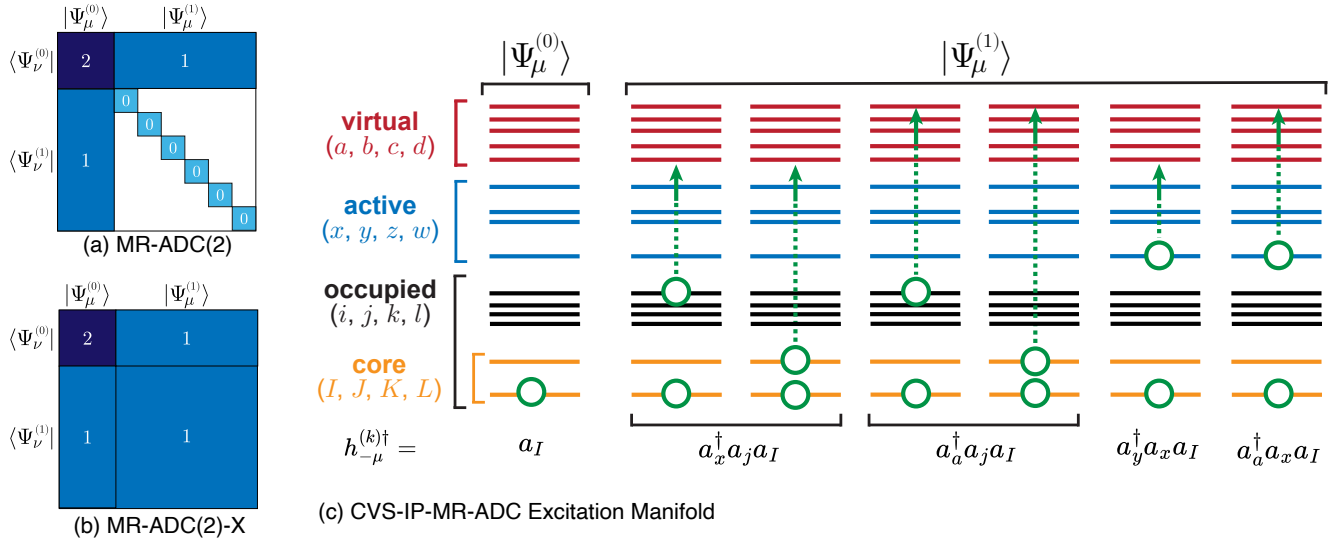


Figure 1: Schematic representation of the effective Hamiltonian matrix  $\mathbf{M}_-$  for the (a) CVS-IP-MR-ADC(2) and (b) CVS-IP-MR-ADC(2)-X approximations in the basis of electronic excitations  $|\Psi_\mu^{(k)}\rangle = h_{-\mu}^{(k)\dagger} |\Psi_0\rangle$  (c). Nonzero matrix blocks are highlighted in color. Numbers represent the perturbation order in which the effective Hamiltonian is evaluated in each matrix block.

operators,  $[A, B] = AB - BA$  and  $[A, B]_+ = AB + BA$  denote commutator and anticommutator, respectively.<sup>24,25,37,38</sup> Eqs. (10) to (12) define the perturbative structure of CVS-IP-MR-ADC matrices, as exemplified in Figure 1 for the  $\mathbf{M}_-$  of strict second-order (CVS-IP-MR-ADC(2)) and extended second-order (CVS-IP-MR-ADC(2)-X) approximations that will be employed in this work.<sup>39,40</sup> Both methods incorporate the single ( $|\Psi_\mu^{(0)}\rangle$ ) and double ( $|\Psi_\mu^{(1)}\rangle$ ) excitations out of the reference wavefunction  $|\Psi_0\rangle$  (described by the  $h_{-\mu}^{(0)\dagger}$  and  $h_{-\mu}^{(1)\dagger}$  operators, respectively), and expand the effective Hamiltonian  $\tilde{H}^{(k)}$  to the second order in the  $\langle\Psi_\nu^{(0)}| - |\Psi_\mu^{(0)}\rangle$  block and to the first order for the  $\langle\Psi_\nu^{(1)}| - |\Psi_\mu^{(0)}\rangle$  and  $\langle\Psi_\nu^{(0)}| - |\Psi_\mu^{(1)}\rangle$  sectors. The CVS-IP-MR-ADC(2)-X method provides a higher-level description of correlation effects in the  $\langle\Psi_\nu^{(1)}| - |\Psi_\mu^{(1)}\rangle$  block by including the contributions from  $\tilde{H}^{(1)}$ , which significantly improve the description of excited-state orbital relaxation effects.

We note that the CVS approximation used in this work is different from the one originally proposed in the context of single-reference ADC methods<sup>72–74</sup> where double excitations from two core orbitals were excluded. Including these doubly excited configurations has been shown to significantly improve the accuracy of CVS approximation<sup>75–77</sup> and has been widely used in other electronic structure methods based on CVS.<sup>78–84</sup>

In our earlier work,<sup>38,39</sup> the CVS-IP-MR-ADC(2) and CVS-IP-MR-ADC(2)-X methods were implemented by deriving Eqs. (10) to (12) in the basis of spin-orbitals  $\psi_p(1) = \phi_p(1)\sigma_p(1)$  where  $\phi_p(1)$  and  $\sigma_p(1)$  are the spatial and spin components of  $\psi_p(1)$ . The resulting working equations can be fully expressed in terms of the one- and antisymmetrized two-electron integrals ( $h_p^q$ ,  $\langle pq||rs\rangle$ ), the energies of non-active orbitals ( $\epsilon_p$ ), the correlation (cluster) amplitudes of effective Hamiltonian and observable operators ( $t_p^{q(k)}$ ,  $t_{pq}^{rs(k)}$ ), and the reduced density matrices of reference wavefunction  $|\Psi_0\rangle$  ( $\gamma_q^p = \langle\Psi_0|a_p^\dagger a_q|\Psi_0\rangle$ ,  $\gamma_{rs}^{pq} = \langle\Psi_0|a_p^\dagger a_q^\dagger a_s a_r|\Psi_0\rangle$ , etc.). However, due to the large computational costs associated with computing, storing, and contracting spin-orbital tensors, the CVS-IP-MR-ADC(2) and CVS-IP-MR-ADC(2)-X calculations were limited to chemical systems with  $\lesssim 300$  spatial orbitals. In Section 2.3, we describe how these bottlenecks can be avoided by formulating CVS-IP-MR-ADC(2) and CVS-IP-MR-ADC(2)-X in the spin-free basis.

### 2.3 Spin-free formulation of CVS-IP-MR-ADC

When using a non-relativistic Hamiltonian, it is possible and computationally advantageous to remove the dependence on spin in equations through so-called spin adaptation. One of the most widely employed approaches to spin-adapt multireference

theories<sup>85,86</sup> is to express all operators in terms of spin-free unitary group generators (e.g.,  $E_{rs}^{pq} = \sum_{\rho\sigma}^{\alpha,\beta} a_{p\rho}^\dagger a_{q\rho}^\dagger a_{s\rho} a_{r\sigma}$ ) that are invariant under the SU(2) transformations of spin-orbitals  $\psi_{p\alpha} \leftrightarrow \psi_{p\beta}$  where  $\alpha$  and  $\beta$  indicate the up and down spin, respectively. Once the operators are defined, their matrix elements are derived using the spin-free formulation of Wick's theorem, yielding fully spin-adapted equations.<sup>87</sup> While this approach can be straightforwardly used in state-specific multireference methods, it is less convenient for multistate effective Hamiltonian theories such as MR-ADC where the excited-state spin symmetry or particle number can be different from that of the reference electronic state.

In this work, we employ the spin adaptation approach developed by Kutzelnigg, Shamasundar, and Mukherjee<sup>85,86,88,89</sup> (KSM) that allows to eliminate spin variables from spin-orbital equations *a posteriori*, by utilizing the relationships between spin-free and spin-dependent tensors for the  $M_S = 0$  reference state. Importantly, the resulting equations can be used to perform spin-adapted calculations starting with a closed- ( $S = 0$ ) or open-shell ( $S > 0$ ) reference state, as long as the reference wavefunction is an equally weighted ensemble of the entire spin multiplet ( $\{|\Psi_0^{S,M_S}\rangle\}$ ,  $M_S = -S, \dots, S$ ). Such reference state can be computed using the state-averaged CASSCF method, which is available in many quantum chemistry software packages. In addition to its straightforward implementation, the KSM approach enforces the  $M_S$  degeneracy of computed open-shell excited states, which can be violated in calculations with a pure-state open-shell reference. The KSM spin adaptation was successfully used to develop efficient implementations of several effective Hamiltonian theories, such as state-specific partially internally contracted multireference coupled cluster theory,<sup>90,91</sup> multireference equation-of-motion coupled cluster theory,<sup>92,93</sup> anti-Hermitian contracted Schrödinger equation,<sup>94-97</sup> and multireference driven similarity renormalization group.<sup>98</sup>

Starting with the  $M_S = 0$  reference wavefunction ( $|\Psi_0\rangle$ ), we spin-adapt  $\mathbf{M}_-$ ,  $\mathbf{T}_-$ , and  $\mathbf{S}_-$  (Eqs. (10) to (12)) using the following relationships for the non-active orbital energies ( $\epsilon_p$ ), the one- and antisymmetrized two-electron integrals ( $h_p^q$ ,  $\langle pq||rs\rangle$ ), and the amplitudes of effective operators  $\tilde{H}^{(k)}$  and  $\tilde{a}_p^{(k)}$  ( $t_p^{q(k)}$ ,  $t_{pq}^{rs(k)}$ ):

$$\epsilon_{p\alpha} = \epsilon_{p\beta} = \epsilon_p, \quad (13)$$

$$h_{p\alpha}^{q\alpha} = h_{p\beta}^{q\beta} = h_p^q, \quad (14)$$

$$\langle p_\alpha q_\beta || r_\alpha s_\beta \rangle = \langle p_\beta q_\alpha || r_\beta s_\alpha \rangle = v_{pq}^{rs}, \quad (15)$$

$$\langle p_\alpha q_\alpha || r_\alpha s_\alpha \rangle = \langle p_\beta q_\beta || r_\beta s_\beta \rangle = v_{pq}^{rs} - v_{pq}^{sr}, \quad (16)$$

$$t_{p\alpha}^{q\alpha(k)} = t_{p\beta}^{q\beta(k)} = t_p^{q(k)}, \quad (17)$$

$$t_{p_\alpha q_\beta}^{r_\alpha s_\beta(k)} = t_{p_\beta q_\alpha}^{r_\beta s_\alpha(k)} = t_{pq}^{rs(k)}, \quad (18)$$

$$t_{p_\alpha q_\alpha}^{r_\alpha s_\alpha(k)} = t_{p_\beta q_\beta}^{r_\beta s_\beta(k)} = t_{pq}^{rs(k)} - t_{pq}^{sr(k)}, \quad (19)$$

where the r.h.s. of each equation is written in terms of spin-free tensors  $\epsilon_p$ ,  $h_p^q$ ,  $v_{pq}^{rs}$ ,  $t_p^{q(k)}$ , and  $t_{pq}^{rs(k)}$ .

Additionally,  $\mathbf{M}_-$ ,  $\mathbf{T}_-$ , and  $\mathbf{S}_-$  depend on up to four-particle active-space reduced density matrices of  $|\Psi_0\rangle$  ( $n$ -RDM,  $1 \leq n \leq 4$ ). The relationships between spin-orbital ( $\gamma$ ) and spin-free ( $\Gamma$ ) RDMs up to  $n = 3$  have been previously reported.<sup>86</sup> For the 1- and 2-RDMs, these equations can be written as:

$$\gamma_{q\alpha}^{p\alpha} = \gamma_{q\beta}^{p\beta} = \frac{1}{2}\Gamma_q^p, \quad (20)$$

$$\gamma_{r_\alpha s_\alpha}^{p_\alpha q_\alpha} = \gamma_{r_\beta s_\beta}^{p_\beta q_\beta} = \frac{1}{6}\Gamma_{rs}^{pq} - \frac{1}{6}\Gamma_{sr}^{pq}, \quad (21)$$

$$\gamma_{r_\alpha s_\beta}^{p_\alpha q_\beta} = \gamma_{r_\beta s_\alpha}^{p_\beta q_\alpha} = \frac{1}{3}\Gamma_{rs}^{pq} + \frac{1}{6}\Gamma_{sr}^{pq}, \quad (22)$$

$$\gamma_{r_\beta s_\alpha}^{p_\alpha q_\beta} = \gamma_{r_\alpha s_\beta}^{p_\beta q_\alpha} = -\left(\frac{1}{6}\Gamma_{rs}^{pq} + \frac{1}{3}\Gamma_{sr}^{pq}\right). \quad (23)$$

For  $n = 3$ , these relationships are rather complicated and can be found in the Supplementary Information.<sup>86</sup> To the best of our knowledge, the equations for spin-adapting 4-RDM have not been published. We derived them using the approach outlined in Ref. 86 and included in the Supplementary Information. We note that the IP-MR-ADC(2) and IP-MR-ADC(2)-X methods can be implemented without 4-RDM by factorizing its contributions into intermediates,<sup>38</sup> although we have not taken advantage of this yet in our efficient implementation.

Finally, the CVS-IP-MR-ADC(2) and CVS-IP-MR-ADC(2)-X equations can be further simplified by taking advantage of spin symmetry in the excitation manifold  $h_{-\mu}^{(k)\dagger} |\Psi_0\rangle$  (Figure 1) for the  $M_S = 0$  reference state. For example, when calculating the matrix-vector products  $\sigma_- = \mathbf{M}_- \mathbf{Z}_-$  for an arbitrary vector  $\mathbf{Z}_-$ , the  $\sigma_{-\mu}$  matrix elements need to be evaluated only for the following excitations:

$$h_{-\mu}^{(0)\dagger} \in \{a_{I_\alpha}\}, \quad (24)$$

$$\begin{aligned}
h_{-\mu}^{(1)\dagger} \in \{ & a_{I_\alpha J_\alpha}^{x_\alpha}, a_{I_\alpha J_\beta}^{x_\beta}; a_{I_\alpha j_\alpha}^{x_\alpha}, a_{I_\alpha j_\beta}^{x_\beta}, a_{I_\beta j_\alpha}^{x_\beta}; \\
& a_{I_\alpha J_\alpha}^{a_\alpha}, a_{I_\alpha J_\beta}^{a_\beta}; a_{I_\alpha j_\alpha}^{a_\alpha}, a_{I_\alpha j_\beta}^{a_\beta}, a_{I_\beta j_\alpha}^{a_\beta}; \\
& a_{I_\alpha x_\alpha}^{y_\alpha}, a_{I_\alpha x_\beta}^{y_\beta}, a_{I_\beta x_\alpha}^{y_\beta}; a_{I_\alpha x_\alpha}^{a_\alpha}, a_{I_\alpha x_\beta}^{a_\beta}, a_{I_\beta x_\alpha}^{a_\beta} \},
\end{aligned}
\tag{25}$$

where we used the index notation from Figure 1c and denoted  $a_{pq}^r \equiv a_r^\dagger a_q a_p$  for brevity. The remaining matrix elements can be obtained, if necessary, by utilizing the spin and permutational symmetry of  $h_{-\mu}^{(k)\dagger} |\Psi_0\rangle$ .

## 3 Implementation

### 3.1 Overview

The CVS-IP-MR-ADC(2) and CVS-IP-MR-ADC(2)-X methods were implemented using Python in the open-source and freely available program Prism.<sup>99</sup> To obtain the CASSCF orbitals, one- and two-electron integrals, and the reference reduced density matrices, Prism was interfaced with the PySCF package.<sup>100</sup> The CVS-IP-MR-ADC code follows an algorithm summarized below:

1. Perform the reference CASSCF calculation for a specified molecular geometry, basis set, and active space using PySCF. Compute the occupied and virtual orbital energies as the eigenvalues of generalized Fock matrix and transform the one- and two-electron integrals to the molecular orbital basis.
2. Compute the  $t_p^{q(1)}$ ,  $t_p^{q(2)}$ , and  $t_{pq}^{rs(1)}$  amplitudes of effective Hamiltonian by solving the amplitude equations as discussed in Ref. 38. The  $t_p^{q(1)}$  and  $t_{pq}^{rs(1)}$  amplitudes parameterize the first-order wavefunction in fully internally contracted second-order N-electron valence perturbation theory (fic-NEVPT2)<sup>31,32</sup> and are used to compute the fic-NEVPT2 correlation energy for the reference state.
3. Evaluate the  $\mathbf{M}_-$  matrix elements in the  $\langle \Psi_\nu^{(0)} | - | \Psi_\mu^{(0)} \rangle$  ( $\mathbf{M}_{-}^{00}$ ) and  $\langle \Psi_\nu^{(1)} | - | \Psi_\mu^{(0)} \rangle$  ( $\mathbf{M}_{-}^{10}/\mathbf{M}_{-}^{01}$ ) sectors (Figure 1). Since the number of single excitations ( $|\Psi_\mu^{(0)}\rangle$ ) is very small (equal to the user-defined number of core orbitals), the  $\mathbf{M}_{-}^{00}$  and  $\mathbf{M}_{-}^{10}/\mathbf{M}_{-}^{01}$  blocks are stored in memory as reusable intermediates for the rest of the calculation.
4. Solve the eigenvalue problem in Eq. (6) by iteratively optimizing the eigenvectors  $\mathbf{Y}_-$  us-

ing the multiroot Davidson algorithm<sup>101</sup> for the requested number of lowest-energy excited states.

5. From the converged eigenvectors  $\mathbf{Y}_-$  compute the spectroscopic amplitudes  $\mathbf{X}_-$  (Eq. (7)) and transition intensities.

Our efficient implementation of CVS-IP-MR-ADC(2) and CVS-IP-MR-ADC(2)-X has several features: (i) spin adaption of all tensor contractions (Section 2.3) assisted by automatic equation and code generation as discussed in Section 3.2; (ii) efficient in-core and out-of-core handling of two-electron integrals utilizing density fitting (Section 3.3) and h5py library;<sup>102</sup> (iii) optimized implementation of tensor contractions using basic linear algebra subroutines (BLAS), opt\_einsum<sup>103</sup> and numpy<sup>104</sup> modules; and (iv) open multiprocessing (OpenMP) parallelization of computationally intensive tasks. In the following, we provide additional details on automatic equation and code generation (Section 3.2) and the use of density fitting (Section 3.3).

### 3.2 Automatic Derivation of Spin-Free Equations and Code Generation

The CVS-IP-MR-ADC(2) and CVS-IP-MR-ADC(2)-X equations are algebraically complicated, which makes their manual implementation tedious and time-consuming. For example, in the spin-orbital basis, the equations for  $\mathbf{M}_{-}^{00}$  contain  $\sim 200$  terms. Due to the lower permutational symmetry of spin-free tensors, the number of spin-adapted  $\mathbf{M}_{-}^{00}$  terms reaches  $\sim 1000$ . In general, spin adaption increases the number of tensor contractions by a factor of 3 to 5, relative to the spin-orbital implementation. As a result, implementing CVS-IP-MR-ADC(2) and CVS-IP-MR-ADC(2)-X efficiently requires assistance from computer software that can derive spin-adapted equations and translate them into optimized code.

Computer-aided derivation and code generation enabled many significant advances in quantum chemistry. Widespread adoption of second quantization formalism<sup>105,106</sup> created a need for tools that can handle tedious operations, such as permuting strings of creation and annihilation operators, normal ordering, evaluating commutators, and matrix elements. Automatic derivation of second-quantized equations was pioneered by Janssen and Schaefer in the framework of

coupled cluster theory (CC).<sup>107</sup> Since then, implementations of many single-<sup>108–125</sup> and multireference methods<sup>91,92,126–131</sup> have been developed with the help of computer tools for equation and code generation, such as tensor contraction engine (TCE),<sup>110</sup> SecondQuantizationAlgebra (SQA),<sup>132</sup> SMITH,<sup>117</sup> SMITH3,<sup>133</sup> ORCA-AGE,<sup>134</sup> sympy,<sup>135</sup>  $p^\dagger q$ ,<sup>136</sup> WICK&D,<sup>137</sup> and QC-MATH.<sup>138,139</sup>

In our spin-orbital implementation of MR-ADC methods, we utilized the SQA program<sup>132</sup> to derive expressions for the elements of  $\mathbf{M}_\pm$ ,  $\mathbf{T}_\pm$ ,  $\mathbf{S}_\pm$ , and their matrix-vector products.<sup>35,37,38</sup> In this work, we developed an extension of SQA called SQA+<sup>140</sup> that allows to perform spin adaptation using the KSM approach discussed in Section 2.3. In SQA+, every operator is initially represented in a spin-orbital form with separate labels for molecular orbitals and electron spin. The spatial orbitals are classified according to one of the four subspaces shown in Figure 1. Once an operator expression is defined by the user, its matrix elements are evaluated in the spin-orbital form by normal-ordering  $a_{p\sigma}^\dagger$  and  $a_{p\sigma}$  ( $\sigma \in \{\alpha, \beta\}$ ) with respect to  $|\Psi_0\rangle$ <sup>37</sup> and discarding vanishing terms. The spin-orbital tensor contractions are converted to the spin-free form using the KSM relationships from Section 2.3 and Supplementary Information, and are simplified by combining identical terms. The resulting expressions are converted into Python code, which can be directly incorporated into Prism. Additionally, SQA+ allows to rewrite the spin-free equations in terms of automatically defined reusable intermediates,<sup>35</sup> which can be used to make the code more efficient. We note that an implementation of spin-free unitary group generators in SQA has been developed by Saitow et al.,<sup>128</sup> although we did not employ it in our work.

### 3.3 Density Fitting

To enable the CVS-IP-MR-ADC calculations with large one-electron basis sets, our efficient implementation utilized the density fitting (DF) approximation<sup>141–145</sup>

$$v_{pq}^{rs} = (pr|qs) \approx \sum_Q^{N_{\text{aux}}} b_{pr}^Q b_{qs}^Q, \quad (26)$$

where the two-electron integrals  $(pr|qs)$  in Chemists’ notation are expressed as a product of three-index tensors  $b_{pq}^Q$  evaluated in the basis of

spatial molecular orbitals ( $\phi_p$ ) and auxiliary basis functions ( $\chi_Q$ ):

$$b_{pq}^Q = \sum_P^{N_{\text{aux}}} (pq|P)(J^{-\frac{1}{2}})_{PQ}, \quad (27)$$

$$(pq|P) = \iint \phi_p(1)\phi_q(1)\frac{1}{r_{12}}\chi_P(2)dr_1dr_2, \quad (28)$$

$$J_{PQ} = \iint \chi_P(1)\frac{1}{r_{12}}\chi_Q(2)dr_1dr_2. \quad (29)$$

The DF approximation lowers the cost of transforming two-electron integrals from atomic to molecular basis and allows to avoid storing  $v_{pq}^{rs}$  on disk, which becomes prohibitively expensive in calculations with more than 1000 molecular orbitals. Density fitting has been widely used to reduce the cost of excited-state electronic structure methods.<sup>146–155</sup> Here, we employ it for the first time in the implementation of MR-ADC.

To assess the accuracy of DF approximation in the CVS-IP-MR-ADC calculations, we computed core ionization energies for molecules from the benchmark set of Liu et al.<sup>156</sup> The results presented in the Supplementary Information demonstrate that using the exact  $v_{pq}^{rs}$  in the reference CASSCF calculations and DF-approximated two-electron integrals in CVS-IP-MR-ADC has a very small effect on core ionization energies with mean absolute error (MAE) of 0.0002 eV. Introducing the DF approximation in the CASSCF step increases the MAE to 0.0011 eV. Overall, these results suggest that DF can be used to significantly lower the cost of CVS-IP-MR-ADC calculations without compromising their accuracy.

## 4 Computational Details

In order to demonstrate the capabilities of CVS-IP-MR-ADC methods, we performed the calculations of core-ionized states and XPS spectra for four molecules: ethyl-ferrocene (EtFC), vinyl-ferrocene (VFC), ethynyl-ferrocene (EFC), and azobenzene. For azobenzene, three structures were investigated: the equilibrium geometries of *trans*- and *cis*-isomers, and the geometry of minimum energy conical intersection (MECI) between the two lowest-energy singlet states ( $S_0$  and  $S_1$ ) that is important in the *trans-cis* photoisomerization. For brevity, we do not include CVS-IP in the abbreviation of MR-ADC methods henceforth.

The ground-state geometries of all molecules

were optimized using density functional theory (DFT)<sup>157–160</sup> with the B3LYP hybrid exchange-correlation functional<sup>161–164</sup> and the D3(BJ) dispersion correction.<sup>165</sup> To compute the  $S_0$ – $S_1$  MECI geometry of azobenzene, we performed state-averaged complete active space self-consistent field<sup>166–168</sup> calculation with equal weights for  $S_0$  and  $S_1$  (SA2-CASSCF). All geometry optimization calculations were performed using the cc-pVQZ basis set with JK density fitting<sup>169–171</sup> in the Molpro<sup>172–174</sup> package.

Reference wavefunctions for the MR-ADC calculations were computed using CASSCF implemented in the PySCF package.<sup>100</sup> For EtFC, active space consisted of 8 electrons in 8 orbitals (CAS(8e,8o)) with significant contributions from the  $\pi^*$  orbitals of cyclopentadienyl rings and the  $d_\pi$  and  $d_\delta$  orbitals of Fe. In the case of VFC and EFC, one additional bonding and antibonding orbital for each  $\pi$ -bond in the substituent were included, resulting in the CAS(10e,10o) and CAS(12e,12o) active spaces, respectively. All azobenzene calculations were performed using CAS(16e,15o), which incorporated the  $\pi$  and  $\pi^*$  orbitals of phenyl rings, the N–N  $\pi$  and  $\pi^*$  orbitals, and one occupied orbital representing nitrogen lone pairs. The active orbitals for all molecules are visualized in the Supporting Information. In addition to the ground electronic state, the CASSCF and MR-ADC calculations of azobenzene were performed for the  $n\pi^*$  excited state at the *trans* ( $C_{2h}$  symmetry) and *cis* ( $C_2$ ) geometries labeled as  $1^1B_u$  and  $1^1B$ , respectively. For the *trans*-isomer, we also considered the  $\pi\pi^*$  excited state of  $1^1B_g$  symmetry. For the MECI geometry ( $C_1$  symmetry), the MR-ADC calculations were performed for the  $S_0$  and  $S_1$  reference wavefunctions obtained from the SA2-CASSCF calculation with equal weights for each electronic state.

The core ionization energies and XPS spectra were computed using the efficient implementation of MR-ADC in the Prism program.<sup>99</sup> As discussed in Section 3, Prism was interfaced with PySCF to obtain the CASSCF orbitals, one- and two-electron integrals, and reference reduced density matrices. All MR-ADC calculations employed the correlation-consistent core-polarized cc-pwCVQZ basis set for carbon and nitrogen<sup>175–177</sup> and the cc-pVQZ basis for hydrogen and iron. Density fitting was used for the reference CASSCF and excited-state MR-ADC methods utilizing the cc-pwCVQZ-JKFIT<sup>169,171</sup> and cc-pwCVQZ-RIFIT<sup>169,178</sup> auxiliary basis sets, respectively. The MR-ADC calcula-

tions were performed using the  $\eta_s = 10^{-6}$  and  $\eta_d = 10^{-10}$  parameters to remove linearly dependent semiinternal and double excitations, respectively.<sup>37</sup> Scalar relativistic effects were incorporated using the spin-free exact-two-component (X2C) Hamiltonian.<sup>156,179–182</sup> The experimental spectra were digitized using WebPlotDigitizer.<sup>183</sup>

## 5 Results and Discussion

### 5.1 Substituted Ferrocenes

We first apply the efficient MR-ADC implementation developed in this work to three ferrocene derivatives with the ethyl (Et), vinyl (V), or ethynyl (E) substituent (R) in one of the cyclopentadienyl (Cp) rings (Figure 2). The redox potentials of these molecules are highly sensitive to the R group, making them attractive surface modifiers for metals and semiconductors in memory devices, electrochemical sensors, batteries, and fuel cells.<sup>185–189</sup> Meanwhile, the properties of ferrocene and its derivatives are known to be strongly influenced by electron correlation effects and have been the focus of many theoretical studies.<sup>190–202</sup> The carbon K-edge XPS spectra of EtFC, VFC, and EFC in the gas phase have been measured experimentally,<sup>184</sup> allowing us to test the performance of MR-ADC for these challenging systems.

Figure 2a shows the experimental C K-edge XPS spectrum of ethyl-ferrocene (EtFC)<sup>184</sup> along with the theoretical spectra calculated at the MR-ADC(2) and MR-ADC(2)-X levels of theory. The experimental XPS spectrum shows a broad feature with a maximum at 290.0 eV and a shoulder around 290.5 eV. The MR-ADC(2) and MR-ADC(2)-X calculations reproduce the experimental spectrum quite well when supplied with 0.20 eV broadening. The best agreement with the experiment is shown by MR-ADC(2)-X, which underestimates the band maximum by 0.4 eV and accurately describes the relative energy of the shoulder feature. MR-ADC(2) overestimates the band maximum by 1.4 eV and exhibits a somewhat more pronounced shoulder.

Analyzing the results of MR-ADC calculations reveals that the lowest-energy core-ionized states in the EtFC XPS spectrum are localized on the three C atoms of the substituted Cp ring directly adjacent to the ethyl (R = Et) group (Figure 2a). The energetic stabilization of these states is consistent with increased core-hole screening due to the



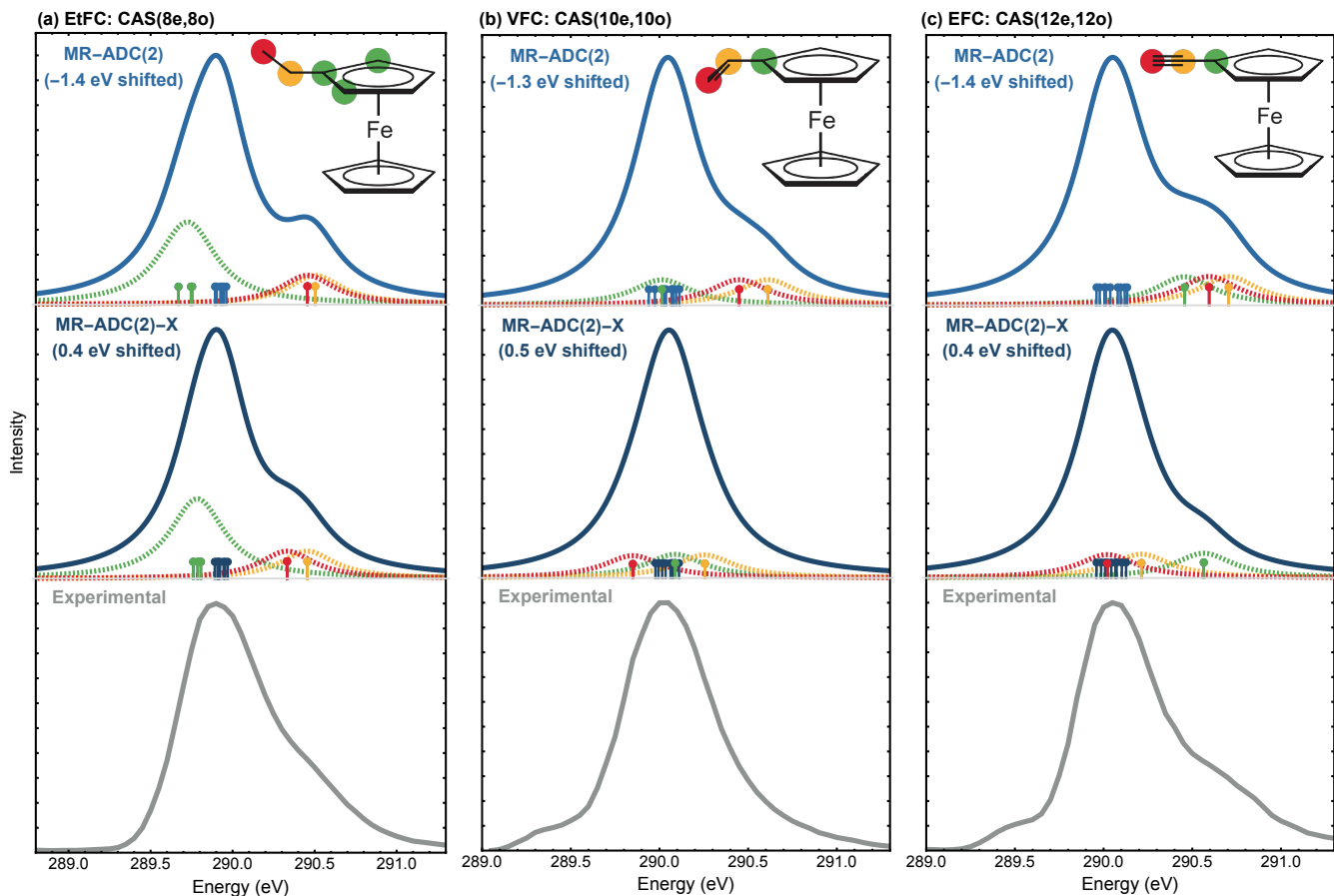
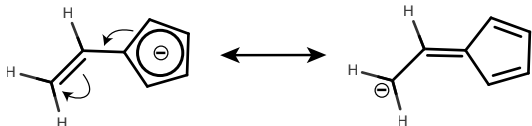


Figure 2: Carbon K-edge XPS spectra of (a) ethyl-ferrocene (EtFC), (b) vinyl-ferrocene (VFC), and (c) ethynyl-ferrocene (EFC) computed using the MR-ADC methods compared to the experimental results.<sup>184</sup> 0.20 eV broadening parameter and were shifted to align with the peak maxima with the those in the experimental spectra. See Section 4 for computational details. Experimental spectra were reprinted from Ref. 184, with the permission of AIP Publishing.

donation of electron density from Et to Cp, as evidenced by the preferential localization of occupied CASSCF natural orbitals on the carbons nearest to Et (Figure S2 of Supporting Information). The core-ionized states localized on the remaining two C atoms of substituted Cp and all carbons of the unsubstituted Cp show very similar ionization energies,  $\sim 0.2$  eV higher than the lowest C K-edge ionization threshold. Together, the Cp carbons give rise to a strong peak observed in the experimental XPS spectrum at 290.0 eV. The shoulder feature at 290.5 eV originates from ionizing the ethyl group, which requires additional  $\sim 0.5$  eV of energy due to the depletion of substituent electron density and less efficient core-hole screening.

Figure 2b presents the experimental<sup>184</sup> and simulated C K-edge XPS spectra of vinyl-ferrocene (VFC). In contrast to EtFC, no shoulder feature with significant intensity is observed at  $\sim 290.5$  eV

in the experimental spectrum, indicating smaller variations in the electronic density of C atoms. A weak shoulder-like feature is seen at  $\sim 289.5$  eV. MR-ADC(2)-X predicts a single spectral band with similar ionization energies for most C atoms. The occupied CASSCF natural orbitals of VFC (Figure S3) exhibit a  $\pi$ -delocalization of electron density between the vinyl group and substituted Cp ring, resulting in a more even core-hole screening among the C K-edge ionized states. The largest difference in the K-edge ionization energy is observed between the  $\text{CH}_2$  and CH groups of the vinyl substituent (Figure 2b), which give rise to the lowest- and highest-energy transitions in the MR-ADC(2)-X spectrum, respectively. The significant difference in carbon core-hole screening of these groups can be attributed to the resonance



and is consistent with the enhanced  $\pi$ -delocalization of CASSCF natural orbitals (Figure S3). In particular, the ionization of  $\text{CH}_2$  group in the vinyl substituent may be responsible for the appearance of weak shoulder at  $\sim 289.5$  eV in the experimental spectrum,<sup>184</sup> although no clear shoulder is seen in the MR-ADC(2)-X spectrum. MR-ADC(2) overestimates the peak position and spacing relative to the experiment, predicting a weak shoulder feature with the selected broadening parameter. This discrepancy can be attributed to the overestimation of core ionization energy for the terminal carbon atom of the vinyl group and is likely associated with the less accurate description of excited-state orbital relaxation effects in MR-ADC(2) compared to MR-ADC(2)-X.

Finally, we consider the experimental<sup>184</sup> and simulated C K-edge XPS spectra of ethynyl-ferrocene (EFC) shown in Figure 2c. Similar to EtFC, the EFC core ionization spectra exhibit a strong peak followed by a shoulder feature  $\sim 0.5$  eV higher in energy. In addition, a weak shoulder is again observed at  $\sim 289.5$  eV, similar to the one in the VFC spectrum. As for EtFC and VFC, MR-ADC(2)-X has the best agreement with the experiment, slightly underestimating the intensity of shoulder at  $\sim 290.5$  eV. In contrast to EtFC where the  $\sim 290.5$  eV shoulder was assigned to the C atom of substituent, the MR-ADC(2)-X calculations suggest that this feature in the EFC spectrum originates from the Cp carbon directly bonded to the ethynyl group. These results suggest that ethynyl acts as an acceptor, depleting the electron density on the Cp carbon adjacent to the substituent and weakening the screening of corresponding core-ionized state. Indeed, the analysis of CASSCF natural orbitals (Figure S4) shows a significant occupation of in-plane and out-of-plane  $\pi$ -antibonding ethynyl orbitals, indicating noticeable back-donation from Cp to the ethynyl group. MR-ADC(2) shows a larger error in the peak maximum and predicts a more intense shoulder than what is observed in the experiment as a result of overestimating the relative energy of core-hole states in the substituent. As for VFC, the MR-ADC methods do not predict a weak shoulder at  $\sim 289.5$  eV, which was assigned to the terminal carbon of ethynyl group in the experimental study.<sup>184</sup> Although this error may be associated

with insufficient description of orbital relaxation effects, it may also originate from the lack of vibrational effects in the simulation and requires further study.

Overall, our results demonstrate that the efficient MR-ADC implementation developed in this work can routinely simulate the K-edge XPS spectra of transition metal complexes with large basis sets. Specifically, the MR-ADC(2) and MR-ADC(2)-X calculations reported here were performed correlating all electrons in 1412 (EFC), 1472 (VFC), and 1532 (EtFC) molecular orbitals. Using a single Intel Xeon Gold 6148 computer node with 40 CPUs, the wall time of MR-ADC(2) and MR-ADC(2)-X simulations did not exceed 4 and 40 hours, respectively, after completing the reference CASSCF calculations. Consistent with our earlier benchmarks,<sup>39,40</sup> the MR-ADC(2)-X results are in very good agreement with the experimental gas-phase XPS spectra.

## 5.2 Azobenzene Photoisomerization

As a multireference approach, MR-ADC is well suited for predicting and interpreting the transient spectra in TR-XPS measurements where X-ray or extreme ultraviolet light is used to probe the electronic structure and molecular dynamics in an excited state populated with a UV/Vis pump photon. We have recently demonstrated this capability by simulating the transient XPS spectra of  $\text{Fe}(\text{CO})_5$  and its photodissociation products ( $\text{Fe}(\text{CO})_4$ ,  $\text{Fe}(\text{CO})_3$ ) following the excitation with 266 nm pump where MR-ADC provided insights into the origin of chemical shifts observed in the experiment.<sup>203</sup>

Here, we use our efficient implementation of MR-ADC to simulate the ground- and excited-state XPS signatures along the photoisomerization of azobenzene ( $(\text{C}_6\text{H}_5)_2\text{N}_2$ ). Azobenzene is a photoswitch molecule that converts from the lowest-energy *trans*- to the higher-energy *cis*-isomer upon irradiation with ultraviolet ( $\sim 365$  nm) light.<sup>204–206</sup> The precise mechanism of *trans-cis* photoisomerization has been a matter of debate,<sup>204,207–212</sup> with some studies suggesting that it involves initial excitation to the  $\pi\pi^*$  excited state, followed by rapid internal conversion to the  $n\pi^*$  potential energy surface where the isomerization can take place.<sup>213–220</sup> Time-resolved photoelectron spectroscopy (TR-PES) measurements in the UV region of electromagnetic spectrum provided valu-

able insights about the mechanism of this photoisomerization.<sup>204</sup> Complimentary to TR-PES, TR-XPS can help to elucidate this mechanism further by detecting the element-specific transient spectral signatures along the course of photochemical reaction. Although no experimental TR-XPS studies have been presented to date, the ground-state carbon and nitrogen K-edge XPS spectra of *trans*-azobenzene in the gas phase have been recently reported.<sup>221</sup> In addition to TR-XPS, time-resolved X-ray absorption spectroscopy has been proposed and theoretically evaluated as a technique for studying azobenzene photoisomerization.<sup>222,223</sup>

We performed the MR-ADC(2)-X calculations of XPS spectra at three azobenzene geometries: the equilibrium structures of *trans*- and *cis*-isomers and the geometry of minimum energy conical intersection (MECI) between the two lowest-energy singlet states that is believed to be important in photoisomerization (Section 4).<sup>210,219,224</sup> For each structure, the carbon and nitrogen K-edge XPS signatures were simulated for the ground ( $S_0$ ) and lowest-energy excited ( $S_1$ ) singlet states. For the *trans*- and *cis*-isomers, the  $S_1$  state corresponds to the  $n\pi^*$  excitation from the molecular orbital localized on nitrogen lone pairs to the lowest-energy  $\pi$ -antibonding orbital of the molecule (Figures 4b, S6, S9). We also computed the XPS spectra of *trans*-azobenzene in the second singlet excited state ( $S_2$ ) corresponding to the  $\pi\pi^*$  electronic transition (Figures 4c and S7). The calculations employed large quadruple-zeta basis sets correlating all electrons in 1476 molecular orbitals and CAS(16e,15o). Additional computational details can be found in Section 4 and Supplementary Information. We note that our calculations did not incorporate excited-state relaxation and nuclear dynamics effects that can be important for accurate interpretation of TR-XPS spectra.

Figures 3a to 3c show the simulated C K-edge XPS spectra of *trans*- and *cis*-azobenzene in the  $S_0$ ,  $n\pi^*$ , and  $\pi\pi^*$  electronic states. For the ground state of *trans*-isomer, the results of simulations are in an excellent agreement with the experimental spectrum (Figure 3d) measured by Carlini et al.<sup>221</sup> In all C K-edge XPS spectra, an intense peak is followed by a feature with weaker intensity that appears as a shoulder in the  $S_0$  spectrum. These two features correspond to the K-edge ionization of C atoms in two distinct chemical environments: 1) ten H-bonded C's and 2) two N-bonded C's. Due to increasing electronegativity ( $\chi$ ) in the order  $\chi(\text{H})$

$< \chi(\text{C}) < \chi(\text{N})$ , the N-bonded carbons exhibit a higher charge and less efficient core-hole screening than those attached to the H atoms, resulting in a significant blueshift of the corresponding feature. As can be seen in Figure 3c, the ground-state XPS spectra of *trans*- and *cis*-isomers exhibit nearly identical spacing between the two peaks ( $\sim 0.6$  eV), indicating that the electronic environment of C atoms in these states is similar.

Analyzing the  $n\pi^*$  and  $\pi\pi^*$  C K-edge XPS spectra reveals significant differences in the electronic structure of these excited states. The  $\pi\pi^*$  spectrum is very similar to that of the  $S_0$  state, suggesting that the  $S_0 \rightarrow \pi\pi^*$  transition does not significantly change the electron density distribution around the C atoms of *trans*-azobenzene. In contrast, populating the  $n\pi^*$  state results in  $\sim 0.3$  eV redshift of the lowest-energy peak and  $\sim 0.4$  eV blueshift of the peak with a weaker intensity, increasing their spacing from  $\sim 0.6$  to  $\sim 1.3$  eV in both *trans*- and *cis*-azobenzene. These results are consistent with the analysis of CASSCF natural orbitals (Figure 4) where the  $n\pi^*$  excited state shows a higher delocalization of the  $\pi^*$  ( $4b_g$ ) orbital as compared to that of the  $n$  ( $1a_g$ ) orbital, transferring some electron density into the phenyl rings of azobenzene. On the contrary, the orbitals involved in the  $\pi\pi^*$  excitation are similarly delocalized across the C framework of the molecule. Importantly, the results of calculations demonstrate that the  $\pi\pi^*$  and  $n\pi^*$  states exhibit noticeably different C K-edge XPS spectra at the *trans*-geometry, which may facilitate their spectroscopic identification in the TR-XPS experiments.

Figures 3e to 3g present the N K-edge XPS spectra of *trans*- and *cis*-azobenzene. For each structure and electronic state, the N K-edge spectrum displays a single peak corresponding to the 1s ionization of two symmetry-equivalent nitrogen atoms. The MR-ADC(2)-X method underestimates the experimental core binding energy<sup>221</sup> of *trans*-azobenzene in the  $S_0$  state by  $\sim 0.6$  eV. In contrast to the C K-edge XPS spectra, the computed N K-ionization energies are more sensitive to the *cis/trans*-orientation of ground state geometry or excitation to the  $\pi\pi^*$  state. Specifically, isomerization from *trans*- to *cis*-azobenzene on the  $S_0$  potential energy surface increases the N K-binding energy by  $\sim 0.5$  eV while the  $\pi\pi^*$  excitation at the *trans* geometry decreases it by  $\sim 0.8$  eV. Exciting the molecule to the  $n\pi^*$  state results in  $\sim 0.2$  and  $0.4$  eV blueshifts in peak position for the *trans*- and

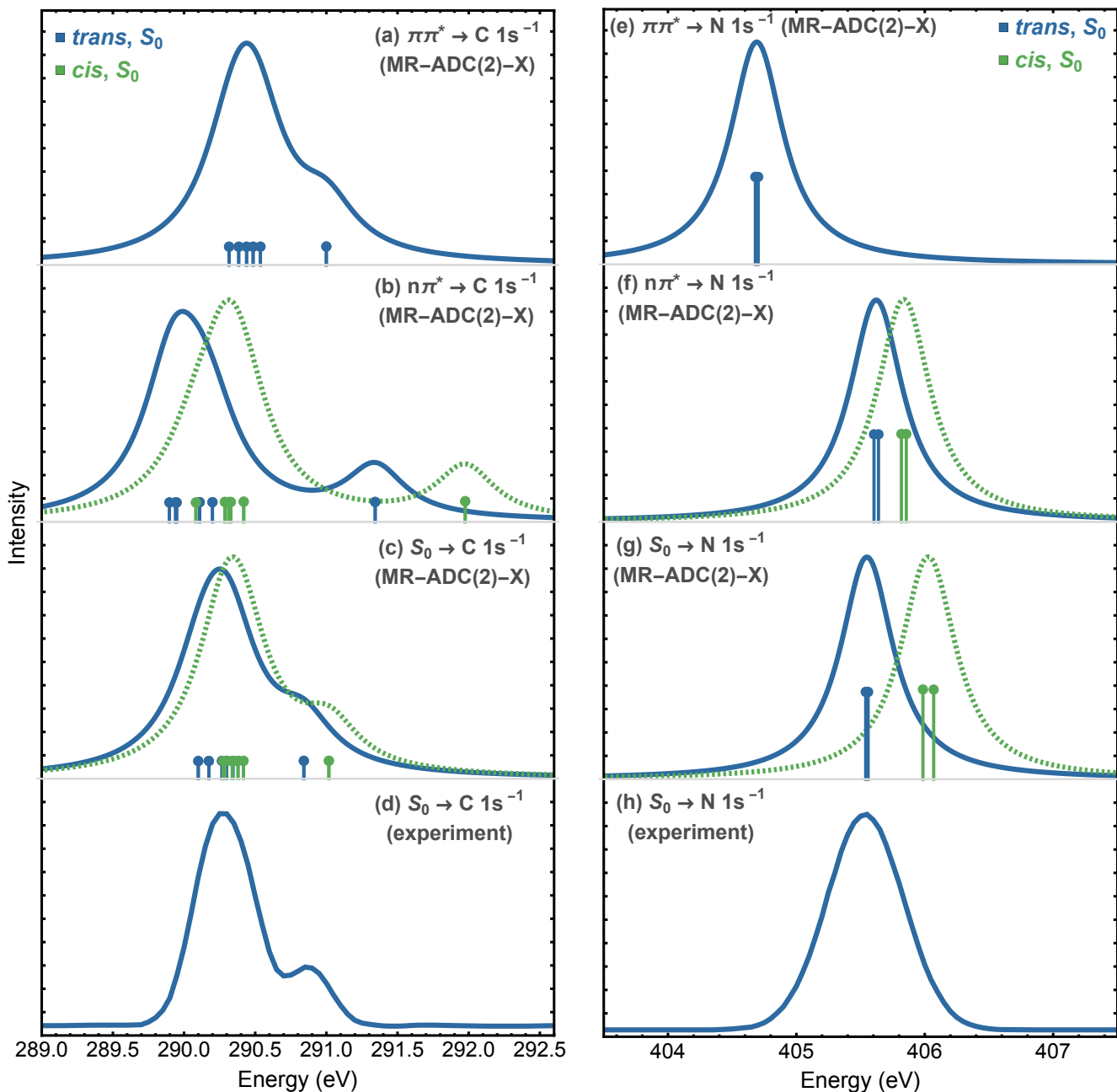


Figure 3: Carbon and Nitrogen K-edge XPS spectra of azobenzene simulated for the  $\pi\pi^*$  excited (a,e),  $n\pi^*$  excited (b,f), and  $S_0$  ground (c,g) states using the MR-ADC(2)-X method. The results are calculated at the *trans* (blue) or *cis* (green) ground-state equilibrium geometries. The simulated spectra were broadened with a 0.25 eV parameter and shifted by 0.85 eV (a-c) or 0.63 eV (e-g). See Section 4 for computational details. Also shown are the experimental  $S_0$  XPS spectra of *trans*-azobenzene (d,h), reprinted from Ref. 221, with the permission of AIP Publishing.

*cis*-isomers, respectively. As for the C K-edge, all spectral changes can be interpreted based on the analysis of CASSCF natural orbitals (Figure 3). For example, the significant ( $\sim 0.8$  eV) blueshift of N K-signal for the  $\pi\pi^*$  state is consistent with

excited-state electron density concentrating on the orbitals localized on the N atoms ( $3a_u$  and  $4b_g$ , Figure 3c) as opposed to the orbitals localized on the phenyl rings ( $4a_u$  and  $5b_g$ ).

Finally, to demonstrate an application of MR-

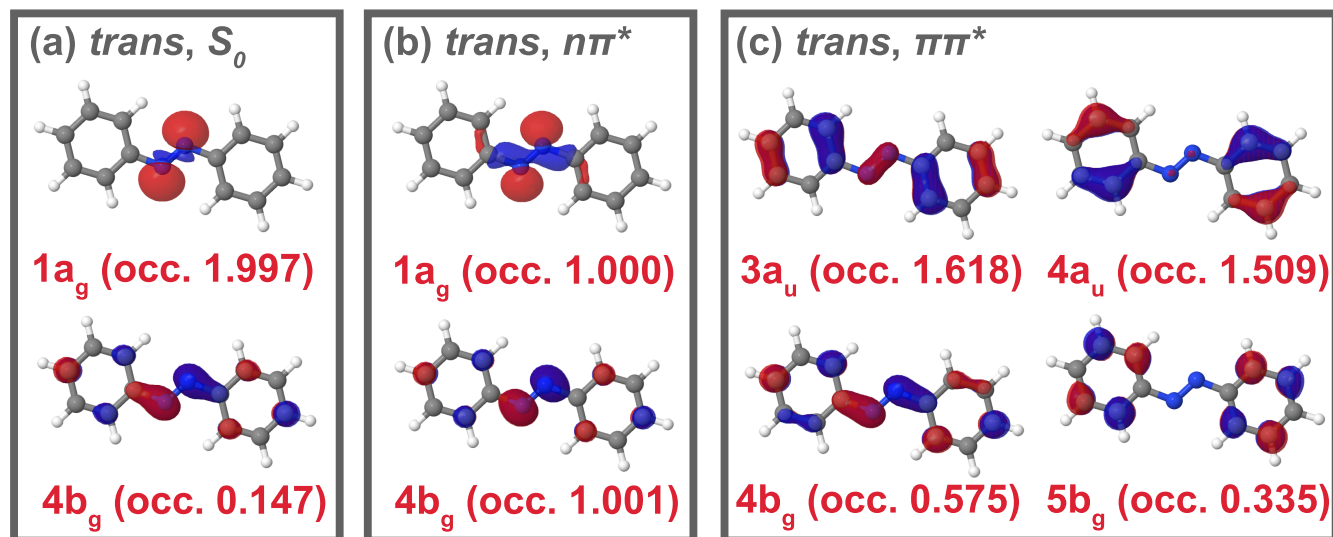


Figure 4: Selected CASSCF natural orbitals and their occupations for the three electronic states of *trans*-azobenzene: (a) ground state ( $S_0$ ), (b)  $n\pi^*$  excited state, and (c)  $\pi\pi^*$  excited state. Calculations were performed using the (16e,15o) active space and the cc-pwCVQZ basis set. See Supplementary Information for the natural orbital plots of remaining active orbitals.

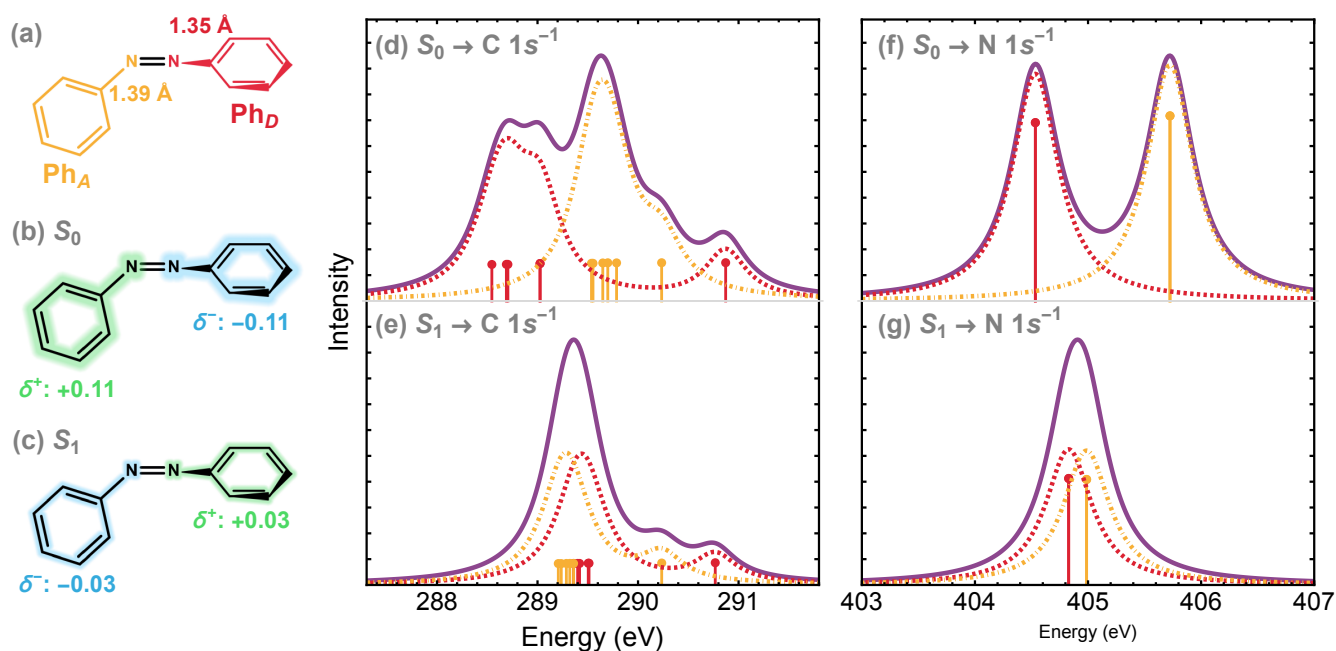


Figure 5: (a) Schematic representation of the azobenzene molecule at the  $S_0$ - $S_1$  minimum energy conical intersection geometry. (b) and (c) Mulliken charges of the  $NPh_A$  and  $NPh_D$  fragments computed for the  $S_0$  and  $S_1$  states, respectively. (d) and (e) C K-edge XPS spectra for the  $S_0$  and  $S_1$  states, respectively. (f) and (g) N K-edge XPS spectra for the  $S_0$  and  $S_1$  states, respectively. All calculations used the SA2-CASSCF(16e,15o) reference wavefunction and the cc-pwCVQZ basis set with X2C relativistic corrections. The spectra were simulated using MR-ADC(2)-X and 0.25 eV broadening parameter.

ADC at non-equilibrium regions of potential energy surfaces, we analyze the XPS spectra computed for the  $S_0$ - $S_1$  MECI geometry shown in Figure 5a. The MECI exhibits an unusual structure of  $C_1$  symme-

try with a  $91.6^\circ$  dihedral angle between the two phenyl rings (Ph) and significantly different N-C bond distances (1.39 and 1.35 Å). As can be seen from the occupations of CASSCF natural orbitals

(Figures S10 and S11), the two singlet states participating in MECI show significantly different degree of open-shell character. Consistent with Ref. 223, we will refer to the state with lower/higher open-shell character as “closed-shell”/“open-shell” and label them as  $S_0/S_1$ . To distinguish between the two non-equivalent NPh fragments, we denote the Ph group with the shorter/longer N–C bond as  $\text{Ph}_D/\text{Ph}_A$ . The Mulliken analysis of charge density (Figure 5b,c) reveals that  $\text{NPh}_D$  has a lower total charge than  $\text{NPh}_A$  in the  $S_0$  state, but a higher charge in the  $S_1$  state.

The C and N K-edge XPS spectra of  $S_0$  and  $S_1$  simulated at the MECI geometry are shown in Figures 5d to 5g. Due to the asymmetric structure, the spectra show distinct XPS signatures for the C and N atoms of the  $\text{NPh}_D$  and  $\text{NPh}_A$  groups of the molecule. In the closed-shell  $S_0$  state, the lowest-energy C and N K-edge ionization occurs in the  $\text{Ph}_D$  fragment, which exhibits significantly higher electron density and more efficient core-hole screening. Ionizing the  $\text{Ph}_A$  group requires  $\sim 1$  eV of additional ionization energy, significantly broadening the C and N K-edge XPS spectra in comparison to those of ground-state azobenzene (Figure 3). The XPS signatures of open-shell  $S_1$  state more closely resemble the ground-state spectra with overlapping peaks originating from  $\text{Ph}_D$  and  $\text{Ph}_A$ . These results are consistent with the analysis of Mulliken charges (Figures 5b and 5c) and CASSCF natural orbitals (Figures S10 and S11), which reveal a more even electron density distribution between  $\text{NPh}_D$  and  $\text{NPh}_A$  in the  $S_1$  state.

Overall, the results of our simulations suggest that TR-XPS can be a useful tool in investigating the photoisomerization of azobenzene molecule, with complementary information provided by the measurements at C and N K-edges. In particular, the C K-edge spectra are expected to help with the detection of molecules in the  $n\pi^*$  excited state and are rather insensitive to their *trans/cis*-orientation. On the contrary, the peak shifts measured in the N K-edge spectra can be useful to identify molecules in the  $\pi\pi^*$  state and to distinguish between the spectral signatures of *trans*- and *cis*-isomers. Monitoring the broadening of C and N K-edge XPS spectra as a function of time may help to provide additional details about the mechanism of photoisomerization. In addition to the XPS spectra for each electronic state (Figures 3 and 5), we computed the difference spectra (Figures S13 to S16) that may be helpful in interpreting the TR-XPS measurements.

We stress, however, that our simulations did not incorporate the excited-state relaxation and nuclear dynamics effects, which can be important for the accurate interpretation of TR-XPS spectra and will be the subject of future work.

## 6 Conclusions

In this work, we presented an efficient implementation of multireference algebraic diagrammatic construction theory with core-valence separation for simulating core-ionized states and X-ray photoelectron spectra (CVS-IP-MR-ADC). Developed in the open-source and freely available Prism program,<sup>99</sup> CVS-IP-MR-ADC takes advantage of spin adaptation, automatic code generation, and efficient handling of two-electron integrals via density fitting. Incorporating dynamic and static correlation, CVS-IP-MR-ADC allows to accurately simulate the X-ray or extreme ultraviolet photoelectron spectra (XPS) for molecules in excited electronic states or at nonequilibrium ground-state geometries. The CVS-IP-MR-ADC is resilient to intruder-state problems and allows to calculate many (10’s or even 100’s) excited states starting with a single CASSCF wavefunction for the reference electronic state.

We demonstrated the capabilities of our efficient CVS-IP-MR-ADC implementation by applying it to substituted ferrocene complexes and azobenzene molecule along its photoisomerization pathway. In all calculations, we used core-polarized quadruple-zeta basis sets, correlating all electrons in more than 1500 molecular orbitals. For the ground electronic states of substituted ferrocenes and *trans*-azobenzene, the carbon K-edge XPS spectra simulated using the extended second-order CVS-IP-MR-ADC method (CVS-IP-MR-ADC(2)-X) are in a very good agreement with experimental measurements. Encouraged by these results, we also computed the carbon and nitrogen K-edge XPS spectra for the azobenzene molecule in its excited states and at the geometry of asymmetric minimum energy conical intersection, which may be useful in interpreting the future time-resolved XPS experiments.

The efficient implementation strategy presented in this work can be used to develop fast MR-ADC methods for simulating other spectroscopic properties, including electron attachment and ionization in the UV/Vis region,<sup>37,38</sup> and neutral excitations in the UV/Vis and X-ray absorption spectroscopies

(XAS).<sup>24,35,36</sup> In addition, spin-orbit coupling effects can be incorporated to enable accurate simulations of L- and M-edge XPS and XAS spectra.<sup>203</sup> These developments will be reported in the forthcoming publications of this series and will further expand the application domain of MR-ADC.

**Acknowledgement** This work was supported by the National Science Foundation, under Grant No. CHE-2044648. The authors would like to thank Nicholas Gaba for testing the CVS-IP-MR-ADC code and valuable suggestions on its improvements. Computations were performed at the Ohio Supercomputer Center under Project No. PAS1583.<sup>225</sup>

## Supporting Information Available

Relationships between spin-orbital and spin-free 3- and 4-RDMs, benchmark of density fitting approximation in the CVS-IP-MR-ADC calculations, geometries of all molecules, CASSCF natural orbitals, tables with XPS ionization energies and spectroscopic factors, and simulated difference XPS spectra for azobenzene.

## References

- (1) Zhang, B.; Sun, L. Artificial photosynthesis: opportunities and challenges of molecular catalysts. *Chem. Soc. Rev.* **2019**, *48*, 2216–2264.
- (2) Öberg, K. I. Photochemistry and Astrochemistry: Photochemical Pathways to Interstellar Complex Organic Molecules. *Chem. Rev.* **2016**, *116*, 9631–9663.
- (3) Hoffmann, N. Photochemical reactions of aromatic compounds and the concept of the photon as a traceless reagent. *Photoch. Photobio. Sci.* **2012**, *11*, 1613–1641.
- (4) Balzani, V.; Bergamini, G.; Ceroni, P. Light: A Very Peculiar Reactant and Product. *Angew. Chem. - Int. Ed.* **2015**, *54*, 11320–11337.
- (5) Bonfield, H. E.; Knauber, T.; Lévesque, F.; Moschetta, E. G.; Susanne, F.; Edwards, L. J. Photons as a 21st century reagent. *Nat. Commun.* **2020**, *11*, 804.
- (6) Twilton, J.; Le, C. C.; Zhang, P.; Shaw, M. H.; Evans, R. W.; MacMillan, D. W. C. The merger of transition metal and photocatalysis. *Nat. Rev. Chem.* **2017**, *1*, 0052.
- (7) Sender, M.; Ziegenbalg, D. Light Sources for Photochemical Processes – Estimation of Technological Potentials. *Chem-ing-tech.* **2017**, *89*, 1159–1173.
- (8) Noël, T.; Gelonch, M. E.; Huvaere, K. *Photochemical Processes in Continuous-Flow Reactors*; Chapter Chapter 9, pp 245–267.
- (9) Coropceanu, V.; Chen, X.-K.; Wang, T.; Zheng, Z.; Brédas, J.-L. Charge-transfer electronic states in organic solar cells. *Nat. Rev. Mater.* **2019**, *4*, 689–707.
- (10) Mai, S.; González, L. Molecular Photochemistry: Recent Developments in Theory. *Angew. Chem. - Int. Ed.* **2020**, *59*, 16832–16846.
- (11) Markushyna, Y.; Savateev, A. Light as a Tool in Organic Photocatalysis: Multi-Photon Excitation and Chromoselective Reactions. *Eur. J. Org. Chem.* **2022**, *2022*, e202200026.
- (12) Srivastava, V.; Singh, P. K.; Singh, P. P. Recent advances of visible-light photocatalysis in the functionalization of organic compounds. *J. Photochem. Photobiol. C Photochem. Rev.* **2022**, *50*, 100488.
- (13) Herzberg, G. *Electronic Spectra and Electronic Structure of Polyatomic Molecules*; Molecular spectra and molecular structure; Van Nostrand: New York, 1966.
- (14) Wörner, H. J.; Merkt, F. In *Handbook of High-resolution Spectroscopy*; Quack, M., Merkt, F., Eds.; Wiley, 2013; Vol. 1; Chapter Fundamentals of Electronic Spectroscopy, pp 175–262.
- (15) Marek, M. S.; Backup, T.; Southall, J.; Cogdell, R. J.; Motzkus, M. Highlighting short-lived excited electronic states with pump-degenerate-four-wave-mixing. *J. Chem. Phys.* **2013**, *139*, 074202.
- (16) Garcia Ruiz, R.; Berger, R.; Billowes, J.; Binnersley, C.; Bissell, M.; Breier, A.; Brinson, A.; Chrysalidis, K.; Cocolios, T.

- Cooper, B. et al. Spectroscopy of short-lived radioactive molecules. *Nature* **2020**, *581*, 396–400.
- (17) Gaffney, K. J. Capturing photochemical and photophysical transformations in iron complexes with ultrafast X-ray spectroscopy and scattering. *Chem. Sci.* **2021**, *12*, 8010–8025.
- (18) Reinhard, M. E.; Mara, M. W.; Kroll, T.; Lim, H.; Hadt, R. G.; Alonso-Mori, R.; Chollet, M.; Glowina, J. M.; Nelson, S.; Sokaras, D. et al. Short-lived metal-centered excited state initiates iron-methionine photodissociation in ferrous cytochrome c. *Nat. Commun.* **2021**, *12*, 1086.
- (19) Polli, D.; Altoè, P.; Weingart, O.; Spillane, K. M.; Manzoni, C.; Brida, D.; Tomasello, G.; Orlandi, G.; Kukura, P.; Mathies, R. A. et al. Conical intersection dynamics of the primary photoisomerization event in vision. *Nature* **2010**, *467*, 440–443.
- (20) Neville, S. P.; Chergui, M.; Stolow, A.; Schurman, M. S. Ultrafast x-ray spectroscopy of conical intersections. *Phys. Rev. Lett.* **2018**, *120*, 243001.
- (21) Wörner, H. J.; Bertrand, J. B.; Kartashov, D. V.; Corkum, P. B.; Villeneuve, D. M. Following a chemical reaction using high-harmonic interferometry. *Nature* **2010**, *466*, 604–607.
- (22) Ruckebauer, M.; Mai, S.; Marquetand, P.; González, L. Revealing deactivation pathways hidden in time-resolved photoelectron spectra. *Sci. Rep.* **2016**, *6*, 35522.
- (23) Severino, S.; Ziemis, K. M.; Reduzzi, M.; Summers, A.; Sun, H.-W.; Chien, Y.-H.; Gräfe, S.; Biegert, J. Attosecond core-level absorption spectroscopy reveals the electronic and nuclear dynamics of molecular ring opening. *Nat. Photon.* **2024**, 1–7.
- (24) Sokolov, A. Y. Multi-reference algebraic diagrammatic construction theory for excited states: General formulation and first-order implementation. *J. Chem. Phys.* **2018**, *149*, 204113.
- (25) Sokolov, A. Y. Multireference perturbation theories based on the Dyall Hamiltonian. *Advances in Quantum Chemistry* **2024**, <https://doi.org/10.1016/bs.aiq.2024.04.004>.
- (26) Andersson, K.; Malmqvist, P. Å.; Roos, B. O.; Sadlej, A. J.; Wolinski, K. Second-order perturbation theory with a CASSCF reference function. *J. Phys. Chem.* **1990**, *94*, 5483–5488.
- (27) Andersson, K.; Malmqvist, P. Å.; Roos, B. O. Second-order perturbation theory with a complete active space self-consistent field reference function. *J. Chem. Phys.* **1992**, *96*, 1218–1226.
- (28) Hirao, K. Multireference Møller–Plesset method. *Chem. Phys. Lett.* **1992**, *190*, 374–380.
- (29) Finley, J. P.; Malmqvist, P. Å.; Roos, B. O.; Serrano-Andrés, L. The multi-state CASPT2 method. *Chem. Phys. Lett.* **1998**, *288*, 299–306.
- (30) Angeli, C.; Cimiraglia, R. Multireference perturbation CI IV. Selection procedure for one-electron properties. *Theor. Chem. Acc.* **2001**, *105*, 259–264.
- (31) Angeli, C.; Cimiraglia, R.; Malrieu, J.-P. N-electron valence state perturbation theory: a fast implementation of the strongly contracted variant. *Chem. Phys. Lett.* **2001**, *350*, 297–305.
- (32) Angeli, C.; Cimiraglia, R.; Evangelisti, S.; Leininger, T.; Malrieu, J.-P. Introduction of n-electron valence states for multireference perturbation theory. *J. Chem. Phys.* **2001**, *114*, 10252–10264.
- (33) Angeli, C.; Borini, S.; Cestari, M.; Cimiraglia, R. A quasidegenerate formulation of the second order n-electron valence state perturbation theory approach. *J. Chem. Phys.* **2004**, *121*, 4043–4049.
- (34) Granovsky, A. A. Extended multi-configuration quasi-degenerate perturbation theory: The new approach to multi-state multi-reference perturbation theory. *J. Chem. Phys.* **2011**, *134*, 214113.



- (35) Mazin, I. M.; Sokolov, A. Y. Multireference Algebraic Diagrammatic Construction Theory for Excited States: Extended Second-Order Implementation and Benchmark. *J. Chem. Theory Comput.* **2021**, *17*, 6152–6165.
- (36) Mazin, I. M.; Sokolov, A. Y. Core-Excited States and X-ray Absorption Spectra from Multireference Algebraic Diagrammatic Construction Theory. *J. Chem. Theory Comput.* **2023**, *19*, 4991–5006.
- (37) Chatterjee, K.; Sokolov, A. Y. Second-Order Multireference Algebraic Diagrammatic Construction Theory for Photoelectron Spectra of Strongly Correlated Systems. *J. Chem. Theory Comput.* **2019**, *15*, 5908–5924.
- (38) Chatterjee, K.; Sokolov, A. Y. Extended Second-Order Multireference Algebraic Diagrammatic Construction Theory for Charged Excitations. *J. Chem. Theory Comput.* **2020**, *16*, 6343–6357.
- (39) de Moura, C. E. V.; Sokolov, A. Y. Simulating X-ray photoelectron spectra with strong electron correlation using multireference algebraic diagrammatic construction theory. *Phys. Chem. Chem. Phys.* **2022**, *24*, 4769–4784.
- (40) de Moura, C. E. V.; Sokolov, A. Y. Correction: Simulating X-ray photoelectron spectra with strong electron correlation using multireference algebraic diagrammatic construction theory. *Phys. Chem. Chem. Phys.* **2022**, *24*, 8041–8046.
- (41) Fadley, C. X-ray photoelectron spectroscopy: Progress and perspectives. *J. Electron Spectrosc.* **2010**, *178*, 2–32.
- (42) Greczynski, G.; Hultman, L. A step-by-step guide to perform x-ray photoelectron spectroscopy. *J. Appl. Phys.* **2022**, *132*, 011101.
- (43) Greczynski, G.; Haasch, R. T.; Hellgren, N.; Lewin, E.; Hultman, L. X-ray photoelectron spectroscopy of thin films. *Nat. Rev. Methods Primers* **2023**, *3*, 40.
- (44) Stolow, A.; Bragg, A. E.; Neumark, D. M. Femtosecond Time-Resolved Photoelectron Spectroscopy. *Chem. Rev.* **2004**, *104*, 1719–1758.
- (45) Neppl, S.; Gessner, O. Time-resolved X-ray photoelectron spectroscopy techniques for the study of interfacial charge dynamics. *J. Electron Spectrosc.* **2015**, *200*, 64–77.
- (46) Brauße, F.; Goldsztejn, G.; Amini, K.; Boll, R.; Bari, S.; Bomme, C.; Brouard, M.; Burt, M.; de Miranda, B. C.; Düsterer, S. et al. Time-resolved inner-shell photoelectron spectroscopy: From a bound molecule to an isolated atom. *Phys. Rev. A* **2018**, *97*, 043429.
- (47) Roth, F.; Borgwardt, M.; Wenthaus, L.; Mahl, J.; Palutke, S.; Brenner, G.; Mercurio, G.; Molodtsov, S.; Wurth, W.; Gessner, O. et al. Direct observation of charge separation in an organic light harvesting system by femtosecond time-resolved XPS. *Nat. Commun.* **2021**, *12*, 1196.
- (48) Mayer, D.; Lever, F.; Picconi, D.; Metje, J.; Alisauskas, S.; Calegari, F.; Düsterer, S.; Ehlert, C.; Feifel, R.; Niebuhr, M. et al. Following excited-state chemical shifts in molecular ultrafast x-ray photoelectron spectroscopy. *Nat. Commun.* **2022**, *13*, 198.
- (49) Shavorskiy, A.; Schnadt, J.; Knudsen, J. *Ambient Pressure Spectroscopy in Complex Chemical Environments*; Chapter 9, pp 219–248.
- (50) Costantini, R.; Morgante, A.; Dell’Angela, M. Excitation density in time-resolved water window soft X-ray spectroscopies: Experimental constraints in the detection of excited states. *J. Electron Spectrosc.* **2022**, *254*, 147141.
- (51) Ozawa, K.; Yamamoto, S.; D’angelo, M.; Natsui, Y.; Terashima, N.; Mase, K.; Matsuda, I. Enhanced Photoresponsivity of Fullerene in the Presence of Phthalocyanine: A Time-Resolved X-ray Photoelectron Spectroscopy Study of Phthalocyanine/C60/TiO2(110). *J. Phys. Chem.* **2019**, *123*, 4388–4395.
- (52) Roth, F.; Neppl, S.; Shavorskiy, A.; Ar-ion, T.; Mahl, J.; Seo, H. O.; Bluhm, H.;

- Hussain, Z.; Gessner, O.; Eberhardt, W. Efficient charge generation from triplet excitons in metal-organic heterojunctions. *Phys. Rev. B* **2019**, *99*, 020303.
- (53) Arion, T.; Neppl, S.; Roth, F.; Shavorskiy, A.; Bluhm, H.; Hussain, Z.; Gessner, O.; Eberhardt, W. Site-specific probing of charge transfer dynamics in organic photovoltaics. *Appl. Phys. Lett.* **2015**, *106*, 121602.
- (54) Schuurman, M. S.; Blanchet, V. Time-resolved photoelectron spectroscopy: the continuing evolution of a mature technique. *Phys. Chem. Chem. Phys.* **2022**, *24*, 20012–20024.
- (55) Gabalski, I.; Allum, F.; Seidu, I.; Britton, M.; Brenner, G.; Bromberger, H.; Brouard, M.; Bucksbaum, P. H.; Burt, M.; Cryan, J. P. et al. Time-Resolved X-ray Photoelectron Spectroscopy: Ultrafast Dynamics in CS<sub>2</sub> Probed at the S 2p Edge. *J. Phys. Chem. Lett.* **2023**, *14*, 7126–7133.
- (56) Keefer, D.; Cavaletto, S. M.; Rouxel, J. R.; Garavelli, M.; Yong, H.; Mukamel, S. Ultrafast X-Ray Probes of Elementary Molecular Events. *Annu. Rev. Phys. Chem.* **2023**, *74*, 73–97.
- (57) Banerjee, S.; Sokolov, A. Y. Algebraic Diagrammatic Construction Theory for Simulating Charged Excited States and Photoelectron Spectra. *J. Chem. Theory Comput.* **2023**, *19*, 3037–3053.
- (58) Schirmer, J. Beyond the random-phase approximation: A new approximation scheme for the polarization propagator. *Phys. Rev. A* **1982**, *26*, 2395–2416.
- (59) Schirmer, J. Closed-form intermediate representations of many-body propagators and resolvent matrices. *Phys. Rev. A* **1991**, *43*, 4647–4659.
- (60) Mertins, F.; Schirmer, J. Algebraic propagator approaches and intermediate-state representations. I. The biorthogonal and unitary coupled-cluster methods. *Phys. Rev. A* **1996**, *53*, 2140–2152.
- (61) Schirmer, J.; Trofimov, A. B.; Stelter, G. A non-Dyson third-order approximation scheme for the electron propagator. *J. Chem. Phys.* **1998**, *109*, 4734.
- (62) Schirmer, J.; Trofimov, A. B. Intermediate state representation approach to physical properties of electronically excited molecules. *J. Chem. Phys.* **2004**, *120*, 11449–11464.
- (63) Dreuw, A.; Wormit, M. The algebraic diagrammatic construction scheme for the polarization propagator for the calculation of excited states. *WIREs Comput. Mol. Sci.* **2015**, *5*, 82–95.
- (64) Andersson, K.; Roos, B. O.; Malmqvist, P. Å.; Widmark, P.-O. The Cr<sub>2</sub> potential energy curve studied with multiconfigurational second-order perturbation theory. *Chem. Phys. Lett.* **1994**, *230*, 391–397.
- (65) Evangelisti, S.; Daudey, J. P.; Malrieu, J.-P. P. Qualitative intruder-state problems in effective Hamiltonian theory and their solution through intermediate Hamiltonians. *Phys. Rev. A* **1987**, *35*, 4930–4941.
- (66) Evangelista, F. A. A driven similarity renormalization group approach to quantum many-body problems. *J. Chem. Phys.* **2014**, *141*, 054109.
- (67) Dyal, K. G. The choice of a zeroth-order Hamiltonian for second-order perturbation theory with a complete active space self-consistent-field reference function. *J. Chem. Phys.* **1995**, *102*, 4909–4918.
- (68) Fetter, A. L.; Walecka, J. D. *Quantum theory of many-particle systems*; Dover Publications, 2003.
- (69) Dickhoff, W. H.; Van Neck, D. *Many-body theory exposed!: propagator description of quantum mechanics in many-body systems*; World Scientific Publishing Co., 2005.
- (70) Cederbaum, L. S.; Domcke, W.; Schirmer, J. Many-body theory of core holes. *Phys. Rev. A* **1980**, *22*, 206–222.

- (71) Barth, A.; Cederbaum, L. S. Many-body theory of core-valence excitations. *Phys. Rev. A* **1981**, *23*, 1038–1061.
- (72) Angonoa, G.; Walter, O.; Schirmer, J. Theoretical K-shell ionization spectra of N2 and CO by a fourth-order Green’s function method. *J. Chem. Phys.* **1987**, *87*, 6789–6801.
- (73) Schirmer, J.; Thiel, A. An intermediate state representation approach to K-shell ionization in molecules. I. Theory. *J. Chem. Phys.* **2001**, *115*, 10621–10635.
- (74) Thiel, A.; Schirmer, J.; Köppel, H. An intermediate state representation approach to K-shell ionization in molecules. II. Computational tests. *J. Chem. Phys.* **2003**, *119*, 2088–2101.
- (75) Peng, R.; Copan, A. V.; Sokolov, A. Y. Simulating X-ray Absorption Spectra with Linear-Response Density Cumulant Theory. *J. Phys. Chem. A* **2019**, *123*, 1840–1850.
- (76) Brumboiu, I. E.; Fransson, T. Core-hole delocalization for modeling x-ray spectroscopies: A cautionary tale. *J. Chem. Phys.* **2022**, *156*, 214109.
- (77) Herbst, M. F.; Fransson, T. Quantifying the error of the core–valence separation approximation. *J. Chem. Phys.* **2020**, *153*, 054114.
- (78) Wenzel, J.; Wormit, M.; Dreuw, A. Calculating core-level excitations and x-ray absorption spectra of medium-sized closed-shell molecules with the algebraic-diagrammatic construction scheme for the polarization propagator. *J. Comput. Chem.* **2014**, *35*, 1900–1915.
- (79) Coriani, S.; Koch, H. Communication: X-ray absorption spectra and core-ionization potentials within a core-valence separated coupled cluster framework. *J. Chem. Phys.* **2015**, *143*, 181103.
- (80) Liu, J.; Matthews, D.; Coriani, S.; Cheng, L. Benchmark Calculations of K-Edge Ionization Energies for First-Row Elements Using Scalar-Relativistic Core–Valence-Separated Equation-of-Motion Coupled-Cluster Methods. *J. Chem. Theory Comput.* **2019**, *15*, 1642–1651, PMID: 30702889.
- (81) Zheng, X.; Cheng, L. Performance of Delta-Coupled-Cluster Methods for Calculations of Core-Ionization Energies of First-Row Elements. *J. Chem. Theory Comput.* **2019**, *15*, 4945–4955.
- (82) Vidal, M. L.; Feng, X.; Epifanovsky, E.; Krylov, A. I.; Coriani, S. New and Efficient Equation-of-Motion Coupled-Cluster Framework for Core-Excited and Core-Ionized States. *J. Chem. Theory Comput.* **2019**, *15*, 3117–3133.
- (83) Simons, M.; Matthews, D. A. Accurate Core-Excited States via Inclusion of Core Triple Excitations in Similarity-Transformed Equation-of-Motion Theory. *J. Chem. Theory Comput.* **2022**, *18*, 3759–3765.
- (84) Zheng, X.; Zhang, C.; Jin, Z.; Southworth, S. H.; Cheng, L. Benchmark relativistic delta-coupled-cluster calculations of K-edge core-ionization energies of third-row elements. *Phys. Chem. Chem. Phys.* **2022**, *24*, 13587–13596.
- (85) Shamasundar, K. R. Cumulant decomposition of reduced density matrices, multireference normal ordering, and Wicks theorem: A spin-free approach. *J. Chem. Phys.* **2009**, *131*, 174109.
- (86) Kutzelnigg, W.; Shamasundar, K.; Mukherjee, D. Spinfree formulation of reduced density matrices, density cumulants and generalised normal ordering. *Mol. Phys.* **2010**, *108*, 433–451.
- (87) Kutzelnigg, W.; Mukherjee, D. Normal order and extended Wick theorem for a multiconfiguration reference wave function. *J. Chem. Phys.* **1997**, *107*, 432–449.
- (88) Kutzelnigg, W.; Mukherjee, D. Cumulant expansion of the reduced density matrices. *J. Chem. Phys.* **1999**, *110*, 2800–2809.
- (89) Kutzelnigg, W.; Mukherjee, D. Irreducible Brillouin conditions and contracted

- Schrödinger equations for n-electron systems. II. Spin-free formulation. *J. Chem. Phys.* **2002**, *116*, 4787.
- (90) Datta, D.; Kong, L.; Nooijen, M. A state-specific partially internally contracted multireference coupled cluster approach. *J. Chem. Phys.* **2011**, *134*, 214116.
- (91) Datta, D.; Gauss, J. A Non-antisymmetric Tensor Contraction Engine for the Automated Implementation of Spin-Adapted Coupled Cluster Approaches. *J. Chem. Theory Comput.* **2013**, *9*, 2639–2653.
- (92) Datta, D.; Nooijen, M. Multireference equation-of-motion coupled cluster theory. *J. Chem. Phys.* **2012**, *137*, 204107.
- (93) Huntington, L. M. J.; Demel, O.; Nooijen, M. Benchmark Applications of Variations of Multireference Equation of Motion Coupled-Cluster Theory. *J. Chem. Theory Comput.* **2016**, *12*, 114–132.
- (94) Mazziotti, D. A. Contracted Schrödinger equation: Determining quantum energies and two-particle density matrices without wave functions. *Phys. Rev. A* **1998**, *57*, 4219–4234.
- (95) Mazziotti, D. A. Variational reduced-density-matrix method using three-particle  $N$ -representability conditions with application to many-electron molecules. *Phys. Rev. A* **2006**, *74*, 032501.
- (96) Mazziotti, D. A. Anti-Hermitian Contracted Schrödinger Equation: Direct Determination of the Two-Electron Reduced Density Matrices of Many-Electron Molecules. *Phys. Rev. Lett.* **2006**, *97*, 143002.
- (97) Mazziotti, D. A. Anti-Hermitian part of the contracted Schrödinger equation for the direct calculation of two-electron reduced density matrices. *Phys. Rev. A* **2007**, *75*, 022505.
- (98) Li, C.; Evangelista, F. A. Spin-free formulation of the multireference driven similarity renormalization group: A benchmark study of first-row diatomic molecules and spin-crossover energetics. *J. Chem. Phys.* **2021**, *155*, 114111.
- (99) de Moura, C. E. V.; Sokolov, A. Y. Prism, an implementation of electronic structure theories for simulating spectroscopic properties. <https://github.com/sokolov-group/prism>, accessed 2024-05-10.
- (100) Sun, Q.; Zhang, X.; Banerjee, S.; Bao, P.; Barbry, M.; Blunt, N. S.; Bogdanov, N. A.; Booth, G. H.; Chen, J.; Cui, Z.-H. et al. Recent developments in the PySCF program package. *J. Chem. Phys.* **2020**, *153*, 024109.
- (101) Davidson, E. R. The iterative calculation of a few of the lowest eigenvalues and corresponding eigenvectors of large real-symmetric matrices. *J. Comput. Phys.* **1975**, *17*, 87–94.
- (102) Collette, A. *Python and HDF5: Unlocking Scientific Data*; O'Reilly Media, Inc, 2013.
- (103) Smith, D. G. A.; Gray, J. opt\_einsum - A Python package for optimizing contraction order for einsum-like expressions. *J. Open Source Softw.* **2018**, *3*, 753.
- (104) Harris, C. R.; Millman, K. J.; van der Walt, S. J.; Gommers, R.; Virtanen, P.; Cournapeau, D.; Wieser, E.; Taylor, J.; Berg, S.; Smith, N. J. et al. Array programming with NumPy. *Nature* **2020**, *585*, 357–362.
- (105) Dirac, P. A. M. The quantum theory of the emission and absorption of radiation. *Proc. R. Soc. London A.* **1927**, *114*, 243–265.
- (106) Feynman, R. *Statistical Mechanics: A Set Of Lectures*; Advanced Books Classics; Avalon Publishing, 1998.
- (107) Janssen, C. L.; Schaefer, H. F. The automated solution of second quantization equations with applications to the coupled cluster approach. *Theor. Chem. Acc.* **1991**, *79*, 1–42.
- (108) Li, X.; Paldus, J. Automation of the implementation of spin-adapted open-shell coupled-cluster theories relying on the unitary group formalism. *J. Chem. Phys.* **1994**, *101*, 8812–8826.
- (109) Kállay, M.; Surján, P. R. Higher excitations in coupled-cluster theory. *J. Chem. Phys.* **2001**, *115*, 2945–2954.

- (110) Hirata, S. Tensor Contraction Engine: Abstraction and Automated Parallel Implementation of Configuration-Interaction, Coupled-Cluster, and Many-Body Perturbation Theories. *J. Phys. Chem. A* **2003**, *107*, 9887–9897.
- (111) Kállay, M.; Gauss, J. Calculation of excited-state properties using general coupled-cluster and configuration-interaction models. *J. Chem. Phys.* **2004**, *121*, 9257–9269.
- (112) Hirata, S. Higher-order equation-of-motion coupled-cluster methods. *J. Chem. Phys.* **2004**, *121*, 51–59.
- (113) Kállay, M.; Gauss, J. Approximate treatment of higher excitations in coupled-cluster theory. *J. Chem. Phys.* **2005**, *123*, 214105.
- (114) Auer, A. A.; Baumgartner, G.; Bernholdt, D. E.; Bibireata, A.; Choppella, V.; Cociorva, D.; Gao, X.; Harrison, R.; Krishnamoorthy, S.; Krishnan, S. et al. Automatic code generation for many-body electronic structure methods: the tensor contraction engine. *Mol. Phys.* **2006**, *104*, 211–228.
- (115) Kamiya, M.; Hirata, S. Higher-order equation-of-motion coupled-cluster methods for ionization processes. *J. Chem. Phys.* **2006**, *125*, 074111.
- (116) Kamiya, M.; Hirata, S. Higher-order equation-of-motion coupled-cluster methods for electron attachment. *J. Chem. Phys.* **2007**, *126*, 134112.
- (117) Shiozaki, T.; Kamiya, M.; Hirata, S.; Valeev, E. F. Equations of explicitly-correlated coupled-cluster methods. *Phys. Chem. Chem. Phys.* **2008**, *10*, 3358–3370.
- (118) Köhn, A.; Richings, G. W.; Tew, D. P. Implementation of the full explicitly correlated coupled-cluster singles and doubles model CCSD-F12 with optimally reduced auxiliary basis dependence. *J. Chem. Phys.* **2008**, *129*, 201103.
- (119) Kvaal, S. Ab initio quantum dynamics using coupled-cluster. *J. Chem. Phys.* **2012**, *136*, 194109.
- (120) Kvaal, S. Variational formulations of the coupled-cluster method in quantum chemistry. *Mol. Phys.* **2013**, *111*, 1100–1108.
- (121) Nakajima, T.; Katouda, M.; Kamiya, M.; Nakatsuka, Y. NTChem: A high-performance software package for quantum molecular simulation. *Int. J. Quantum Chem.* **2015**, *115*, 349–359.
- (122) Pedersen, T. B.; Kvaal, S. Symplectic integration and physical interpretation of time-dependent coupled-cluster theory. *J. Chem. Phys.* **2019**, *150*, 144106.
- (123) Kjellgren, E. R.; Hedegård, E. D.; Jensen, H. J. A. Triplet excitation energies from multiconfigurational short-range density-functional theory response calculations. *J. Chem. Phys.* **2019**, *151*, 124113.
- (124) Sumita, M.; Yoshikawa, N. Augmented Lagrangian method for spin-coupled wave function. *Int. J. Quantum Chem.* **2021**, *121*, e26746.
- (125) Leitner, J.; Dempwolff, A. L.; Dreuw, A. The fourth-order algebraic diagrammatic construction scheme for the polarization propagator. *J. Chem. Phys.* **2022**, *157*, 184101.
- (126) Das, S.; Mukherjee, D.; Kállay, M. Full implementation and benchmark studies of Mukherjee’s state-specific multireference coupled-cluster ansatz. *J. Chem. Phys.* **2010**, *132*, 074103.
- (127) Hanauer, M.; Köhn, A. Pilot applications of internally contracted multireference coupled cluster theory, and how to choose the cluster operator properly. *J. Chem. Phys.* **2011**, *134*, 204111.
- (128) Saitow, M.; Kurashige, Y.; Yanai, T. Multireference configuration interaction theory using cumulant reconstruction with internal contraction of density matrix renormalization group wave function. *J. Chem. Phys.* **2013**, *139*, 044118.
- (129) Kim, T. D.; Miranda-Quintana, R. A.; Richer, M.; Ayers, P. W. Flexible ansatz for N-body configuration interaction. *Comput. Theor. Chem.* **2021**, *1202*, 113187.

- (130) Guo, Y.; Sivalingam, K.; Kollmar, C.; Neese, F. Approximations of density matrices in N-electron valence state second-order perturbation theory (NEVPT2). II. The full rank NEVPT2 (FR-NEVPT2) formulation. *J. Chem. Phys.* **2021**, *154*, 214113.
- (131) Black, J. A.; Waigum, A.; Adam, R. G.; Shamasundar, K. R.; Köhn, A. Toward an efficient implementation of internally contracted coupled-cluster methods. *J. Chem. Phys.* **2023**, *158*, 134801.
- (132) Neuscammann, E.; Yanai, T.; Chan, G. K.-L. Quadratic canonical transformation theory and higher order density matrices. *J. Chem. Phys.* **2009**, *130*, 124102.
- (133) MacLeod, M. K.; Shiozaki, T. Communication: Automatic code generation enables nuclear gradient computations for fully internally contracted multireference theory. *J. Chem. Phys.* **2015**, *142*, 051103.
- (134) Krupička, M.; Sivalingam, K.; Huntington, L.; Auer, A. A.; Neese, F. A toolchain for the automatic generation of computer codes for correlated wavefunction calculations. *J. Comput. Chem.* **2017**, *38*, 1853–1868.
- (135) Meurer, A.; Smith, C. P.; Paprocki, M.; Čertík, O.; Kirpichev, S. B.; Rocklin, M.; Kumar, A.; Ivanov, S.; Moore, J. K.; Singh, S. et al. SymPy: symbolic computing in Python. *PeerJ Computer Science* **2017**, *3*, e103.
- (136) Rubin, N. C.; DePrince, A. E. p†q: a tool for prototyping many-body methods for quantum chemistry. *Mol. Phys.* **2021**, *119*, e1954709.
- (137) Evangelista, F. A. Automatic derivation of many-body theories based on general Fermi vacua. *J. Chem. Phys.* **2022**, *157*, 064111.
- (138) Quintero-Monsebaiz, R.; Loos, P.-F. Equation generator for equation-of-motion coupled cluster assisted by computer algebra system. *AIP Adv.* **2023**, *13*, 085035.
- (139) Monino, E.; Marie, A.; Loos, P.-F. QCMATH: Mathematica modules for electronic structure calculations. *arXiv* **2023**, <https://doi.org/10.48550/arXiv.2308.14890>, accessed 2024-05-10, submitted 2023-08-31.
- (140) de Moura, C. E. V.; Sokolov, A. Y. SecondQuantizationAlgebra+ (SQA+), Advanced implementation of Second Quantization Algebra. [https://github.com/sokolov-group/sqa\\_plus](https://github.com/sokolov-group/sqa_plus), accessed 2024-05-10.
- (141) Whitten, J. L. Coulombic potential energy integrals and approximations. *J. Chem. Phys.* **1973**, *58*, 4496–4501.
- (142) Dunlap, B. I.; Connolly, J. W. D.; Sabin, J. R. On some approximations in applications of X alpha theory. *J. Chem. Phys.* **1979**, *71*, 3396–3402.
- (143) Vahtras, O.; Almlöf, J.; Feyereisen, M. Integral approximations for LCAO-SCF calculations. *Chem. Phys. Lett.* **1993**, *213*, 514–518.
- (144) Feyereisen, M.; Fitzgerald, G.; Komornicki, A. Use of approximate integrals in ab initio theory. An application in MP2 energy calculations. *Chem. Phys. Lett.* **1993**, *208*, 359–363.
- (145) Dunlap, B. I. Robust and variational fitting. *Phys. Chem. Chem. Phys.* **2000**, *2*, 2113–2116.
- (146) Hättig, C.; Weigend, F. CC2 excitation energy calculations on large molecules using the resolution of the identity approximation. **2000**, *113*, 5154.
- (147) Hättig, C. Structure Optimizations for Excited States with Correlated Second-Order Methods: CC2 and ADC(2). **2005**, *50*, 37–60.
- (148) Győrffy, W.; Shiozaki, T.; Knizia, G.; Werner, H.-J. Analytical energy gradients for second-order multireference perturbation theory using density fitting. *J. Chem. Phys.* **2013**, *138*, 104104.
- (149) Epifanovsky, E.; Zuev, D.; Feng, X.; Khistyayev, K.; Shao, Y.; Krylov, A. I. General implementation of the resolution-of-the-identity and Cholesky representations of electron repulsion integrals within coupled-cluster and equation-of-motion methods:

- Theory and benchmarks. *J. Chem. Phys.* **2013**, *139*, 134105.
- (150) Helmich, B.; Hättig, C. A pair natural orbital based implementation of ADC(2)-x: Perspectives and challenges for response methods for singly and doubly excited states in large molecules. *Comput. Theor. Chem* **2014**, *1040-1041*, 35–44.
- (151) Kumar, D.; Dutta, A. K.; Manohar, P. U. Resolution of the Identity and Cholesky Representation of EOM-MP2 Approximation: Implementation, Accuracy and Efficiency. *J. Chem. Sci.* **2017**, *129*, 1611–1626.
- (152) Mester, D.; Nagy, P. R.; Kállay, M. Reduced-cost second-order algebraic-diagrammatic construction method for excitation energies and transition moments. *J. Chem. Phys.* **2018**, *148*, 094111.
- (153) Herbst, M. F.; Scheurer, M.; Fransson, T.; Rehn, D. R.; Dreuw, A. adcc: A versatile toolkit for rapid development of algebraic-diagrammatic construction methods. *WIREs Comput. Mol. Sci.* **2020**, e1462.
- (154) Liu, J.; Hättig, C.; Höfener, S. Analytical nuclear gradients for electron-attached and electron-detached states for the second-order algebraic diagrammatic construction scheme combined with frozen-density embedding. *J. Chem. Phys.* **2020**, *152*, 174109.
- (155) Banerjee, S.; Sokolov, A. Y. Efficient implementation of the single-reference algebraic diagrammatic construction theory for charged excitations: Applications to the TEMPO radical and DNA base pairs. *J. Chem. Phys.* **2021**, *154*, 074105.
- (156) Liu, W.; Peng, D. Infinite-order quasirelativistic density functional method based on the exact matrix quasirelativistic theory. *J. Chem. Phys.* **2006**, *125*, 044102.
- (157) Hohenberg, P.; Kohn, W. Density functional theory (DFT). *Phys. Rev* **1964**, *136*, B864.
- (158) Kohn, W.; Sham, L. J. Self-Consistent Equations Including Exchange and Correlation Effects. *Phys. Rev.* **1965**, *140*, A1133–A1138.
- (159) Parr, R.; Weitao, Y. *Density-Functional Theory of Atoms and Molecules*; International Series of Monographs on Chemistry; Oxford University Press, 1994.
- (160) Teale, A. M.; Helgaker, T.; Savin, A.; Adamo, C.; Aradi, B.; Arbuznikov, A. V.; Ayers, P. W.; Baerends, E. J.; Barone, V.; Calaminici, P. et al. DFT exchange: sharing perspectives on the workhorse of quantum chemistry and materials science. *Phys. Chem. Chem. Phys.* **2022**, *24*, 28700–28781.
- (161) Vosko, S. H.; Wilk, L.; Nusair, M. Accurate spin-dependent electron liquid correlation energies for local spin density calculations: a critical analysis. *Can. J. Phys.* **1980**, *58*, 1200–1211.
- (162) Lee, C.; Yang, W.; Parr, R. G. Development of the Colle-Salvetti correlation-energy formula into a functional of the electron density. *Phys. Rev. B* **1988**, *37*, 785–789.
- (163) Becke, A. D. Density-functional thermochemistry. III. The role of exact exchange. *J. Chem. Phys.* **1993**, *98*, 5648–5652.
- (164) Stephens, P. J.; Devlin, F. J.; Chabalowski, C. F.; Frisch, M. J. Ab Initio Calculation of Vibrational Absorption and Circular Dichroism Spectra Using Density Functional Force Fields. *J. Phys. Chem.* **1994**, *98*, 11623–11627.
- (165) Grimme, S.; Ehrlich, S.; Goerigk, L. Effect of the damping function in dispersion corrected density functional theory. *J. Comput. Chem.* **2011**, *32*, 1456–1465.
- (166) Werner, H.-J.; Meyer, W. A quadratically convergent multiconfiguration-self-consistent field method with simultaneous optimization of orbitals and CI coefficients. *J. Chem. Phys.* **1980**, *73*, 2342–2356.
- (167) Werner, H.-J. A quadratically convergent MCSCF method for the simultaneous optimization of several states. *J. Chem. Phys.* **1981**, *74*, 5794–5801.
- (168) Knowles, P. J.; Werner, H.-J. An efficient second-order MC SCF method for long configuration expansions. *Chem. Phys. Lett.* **1985**, *115*, 259–267.

- (169) Weigend, F.; Köhn, A.; Hättig, C. Efficient use of the correlation consistent basis sets in resolution of the identity MP2 calculations. *J. Chem. Phys.* **2002**, *116*, 3175–3183.
- (170) Weigend, F. A fully direct RI-HF algorithm: Implementation, optimised auxiliary basis sets, demonstration of accuracy and efficiency. *Phys. Chem. Chem. Phys.* **2002**, *4*, 4285–4291.
- (171) Bross, D. H.; Hill, J. G.; Werner, H.-J.; Peterson, K. A. Explicitly correlated composite thermochemistry of transition metal species. *J. Chem. Phys.* **2013**, *139*, 094302.
- (172) Werner, H.-J.; Knowles, P. J.; Manby, F. R.; Black, J. A.; Doll, K.; Heßelmann, A.; Kats, D.; Köhn, A.; Korona, T.; Kreplin, D. A. et al. The Molpro quantum chemistry package. *J. Chem. Phys.* **2020**, *152*, 144107.
- (173) Werner, H.; Knowles, P. J.; Knizia, G.; Manby, F. R.; Schütz, M. Molpro: a general-purpose quantum chemistry program package. *WIREs Comput. Mol. Sci.* **2012**, *2*, 242–253.
- (174) Werner, H.-J.; Knowles, P. J.; Knizia, G.; Manby, F. R.; Schütz, M.; Celani, P.; Györffy, W.; Kats, D.; Korona, T.; Lindh, R. et al. MOLPRO, version 2023.2, a package of ab initio programs. <https://www.molpro.net>, accessed 2024-05-10.
- (175) Dunning, T. H. Gaussian basis sets for use in correlated molecular calculations. I. The atoms boron through neon and hydrogen. *J. Chem. Phys.* **1989**, *90*, 1007–1023.
- (176) Peterson, K. A.; Dunning, T. H. Accurate correlation consistent basis sets for molecular core–valence correlation effects: The second row atoms Al–Ar, and the first row atoms B–Ne revisited. *J. Chem. Phys.* **2002**, *117*, 10548–10560.
- (177) Balabanov, N. B.; Peterson, K. A. Systematically convergent basis sets for transition metals. I. All-electron correlation consistent basis sets for the 3d elements Sc–Zn. *J. Chem. Phys.* **2005**, *123*, 064107.
- (178) Hättig, C. Optimization of auxiliary basis sets for RI-MP2 and RI-CC2 calculations: Core–valence and quintuple-zeta basis sets for H to Ar and QZVPP basis sets for Li to Kr. *Phys. Chem. Chem. Phys.* **2004**, *7*, 59–66.
- (179) Dyall, K. G. Interfacing relativistic and non-relativistic methods. I. Normalized elimination of the small component in the modified Dirac equation. *J. Chem. Phys.* **1997**, *106*, 9618–9626.
- (180) Kutzelnigg, W.; Liu, W. Quasirelativistic theory equivalent to fully relativistic theory. *J. Chem. Phys.* **2005**, *123*, 241102.
- (181) Ilias, M.; Saue, T. An infinite-order two-component relativistic Hamiltonian by a simple one-step transformation. *J. Chem. Phys.* **2007**, *126*, 064102.
- (182) Cheng, L.; Gauss, J. Analytical evaluation of first-order electrical properties based on the spin-free Dirac-Coulomb Hamiltonian. *J. Chem. Phys.* **2011**, *134*, 244112.
- (183) Rohatgi, A. WebPlotDigitizer. 2024; <https://automeris.io/WebPlotDigitizer.html>.
- (184) Boccia, A.; Lanzilotto, V.; Marrani, A. G.; Stranges, S.; Zanoni, R.; Alagia, M.; Fronzoni, G.; Decleva, P. C–C bond unsaturation degree in monosubstituted ferrocenes for molecular electronics investigated by a combined near-edge x-ray absorption fine structure, x-ray photoemission spectroscopy, and density functional theory approach. *J. Chem. Phys.* **2012**, *136*, 134308.
- (185) Roth, K. M.; Yasserli, A. A.; Liu, Z.; Dabke, R. B.; Malinovskii, V.; Schweikart, K.-H.; Yu, L.; Tiznado, H.; Zaera, F.; Lindsey, J. S. et al. Measurements of Electron-Transfer Rates of Charge-Storage Molecular Monolayers on Si(100). Toward Hybrid Molecular/Semiconductor Information Storage Devices. *J. Am. Chem. Soc.* **2003**, *125*, 505–517.
- (186) Lindsey, J. S.; Bocian, D. F. Molecules for Charge-Based Information Storage. *Acc. Chem. Res.* **2011**, *44*, 638–650.



- (187) Heinze, K.; Lang, H. Ferrocene: Beauty and Function. *Organometallics* **2013**, *32*, 5623–5625.
- (188) Fabre, B. Functionalization of Oxide-Free Silicon Surfaces with Redox-Active Assemblies. *Chem. Rev.* **2016**, *116*, 4808–4849.
- (189) Rauf, U.; Shabir, G.; Bukhari, S.; Albericio, F.; Saeed, A. Contemporary Developments in Ferrocene Chemistry: Physical, Chemical, Biological and Industrial Aspects. *Molecules* **2023**, *28*, 5765.
- (190) Xu, Z.-F.; Xie, Y.; Feng, W.-L.; Schaefer, H. F. Systematic Investigation of Electronic and Molecular Structures for the First Transition Metal Series Metallocenes  $M(C_5H_5)_2$  ( $M = V, Cr, Mn, Fe, Co,$  and  $Ni$ ). *J. Phys. Chem. A* **2003**, *107*, 2716–2729.
- (191) Coriani, S.; Haaland, A.; Helgaker, T.; Jørgensen, P. The Equilibrium Structure of Ferrocene. *ChemPhysChem* **2006**, *7*, 245–249.
- (192) Harding, M. E.; Metzroth, T.; Gauss, J.; Auer, A. A. Parallel Calculation of CCSD and CCSD(T) Analytic First and Second Derivatives. *J. Chem. Theory Comput.* **2008**, *4*, 64–74, PMID: 26619980.
- (193) DeYonker, N. J.; Williams, T. G.; Imel, A. E.; Cundari, T. R.; Wilson, A. K. Accurate thermochemistry for transition metal complexes from first-principles calculations. *J. Chem. Phys.* **2009**, *131*, 024106.
- (194) Phung, Q. M.; Vancoillie, S.; Pierloot, K. A Multiconfigurational Perturbation Theory and Density Functional Theory Study on the Heterolytic Dissociation Enthalpy of First-Row Metallocenes. *J. Chem. Theory Comput.* **2012**, *8*, 883–892, PMID: 26593350.
- (195) Burow, A. M.; Bates, J. E.; Furche, F.; Eshuis, H. Analytical First-Order Molecular Properties and Forces within the Adiabatic Connection Random Phase Approximation. *J. Chem. Theory Comput.* **2014**, *10*, 180–194, PMID: 26579901.
- (196) Wang, X.; Sokolov, A. Y.; Turney, J. M.; Schaefer, H. F. Spin-Adapted Formulation and Implementation of Density Cumulant Functional Theory with Density-Fitting Approximation: Application to Transition Metal Compounds. *J. Chem. Theory Comput.* **2016**, *12*, 4833–4842.
- (197) Yáñez-S, M.; Moya, S. A.; Zúñiga, C.; Cárdenas-Jirón, G. Theoretical assessment of TD-DFT applied to a ferrocene-based complex. *Comput. Theor. Chem.* **2017**, *1118*, 65–74.
- (198) Sand, A. M.; Truhlar, D. G.; Gagliardi, L. Efficient algorithm for multiconfiguration pair-density functional theory with application to the heterolytic dissociation energy of ferrocene. *J. Chem. Phys.* **2017**, *146*, 034101.
- (199) Sayfutyarova, E. R.; Sun, Q.; Chan, G. K.-L.; Knizia, G. Automated Construction of Molecular Active Spaces from Atomic Valence Orbitals. *J. Chem. Theory Comput.* **2017**, *13*, 4063–4078.
- (200) Irfan, A.; Al-Zeidaneen, F. K.; Ahmed, I.; Al-Sehemi, A. G.; Assiri, M. A.; Ullah, S.; Abbas, G. Synthesis, characterization and quantum chemical study of optoelectronic nature of ferrocene derivatives. *B. Mater. Sci.* **2020**, *43*, 1–8.
- (201) Trivedi, R.; Bhattacharyya, P. A theoretical study of ferrocene based on combined configuration interaction singles (CIS) and time-dependent density functional theory (TDDFT) approach. *Phys. Scripta* **2023**, *99*, 015929.
- (202) Wang, F.; Chantler, C. T. Dominant changes in centre Fe atom of decamethyl-ferrocene from ferrocene in methylation. *Theor. Chem. Acc.* **2023**, *142*.
- (203) Gaba, N. P.; de Moura, C. E. V.; Majumder, R.; Sokolov, A. Y. Simulating transient X-ray photoelectron spectra of  $Fe(CO)_5$  and its photodissociation products with multireference algebraic diagrammatic construction theory. *Phys. Chem. Chem. Phys.* **2024**, *26*, 15927–15938.
- (204) Schultz, T.; Quenneville, J.; Levine, B.; Toniolo, A.; Martínez, T. J.; Lochbrunner, S.; Schmitt, M.; Shaffer, J. P.; Zgier-

- ski, M. Z.; Stolow, A. Mechanism and Dynamics of Azobenzene Photoisomerization. *J. Am. Chem. Soc.* **2003**, *125*, 8098–8099.
- (205) Crespi, S.; Simeth, N. A.; König, B. Heteroaryl azo dyes as molecular photoswitches. *Nat. Rev. Chem.* **2019**, *3*, 133–146.
- (206) Jerca, F. A.; Jerca, V. V.; Hoogenboom, R. Advances and opportunities in the exciting world of azobenzenes. *Nat. Rev. Chem.* **2021**, *6*, 51–69.
- (207) Rau, H.; Lueddecke, E. On the rotation-inversion controversy on photoisomerization of azobenzenes. Experimental proof of inversion. *J. Am. Chem. Soc.* **1982**, *104*, 1616–1620.
- (208) Lednev, I. K.; Ye, T.-Q.; Abbott, L. C.; Hester, R. E.; Moore, J. N. Photoisomerization of a Capped Azobenzene in Solution Probed by Ultrafast Time-Resolved Electronic Absorption Spectroscopy. *J. Phys. Chem. A* **1998**, *102*, 9161–9166.
- (209) Lednev, I.; Ye, T.-Q.; Matousek, P.; Towrie, M.; Foggi, P.; Neuwahl, F.; Umaphathy, S.; Hester, R.; Moore, J. Femtosecond time-resolved UV-visible absorption spectroscopy of trans-azobenzene: dependence on excitation wavelength. *Chem. Phys. Lett.* **1998**, *290*, 68–74.
- (210) Conti, I.; Garavelli, M.; Orlandi, G. The Different Photoisomerization Efficiency of Azobenzene in the Lowest  $n\pi^*$  and  $\pi\pi^*$  Singlets: The Role of a Phantom State. *J. Am. Chem. Soc.* **2008**, *130*, 5216–5230.
- (211) Quick, M.; Dobryakov, A. L.; Gerecke, M.; Richter, C.; Berndt, F.; Ioffe, I. N.; Granovsky, A. A.; Mahrwald, R.; Ernsting, N. P.; Kovalenko, S. A. Photoisomerization Dynamics and Pathways of trans- and cis-Azobenzene in Solution from Broadband Femtosecond Spectroscopies and Calculations. *J. Phys. Chem. B* **2014**, *118*, 8756–8771.
- (212) Tavadze, P.; Avendaño Franco, G.; Ren, P.; Wen, X.; Li, Y.; Lewis, J. P. A Machine-Driven Hunt for Global Reaction Coordinates of Azobenzene Photoisomerization. *J. Am. Chem. Soc.* **2018**, *140*, 285–290.
- (213) Cembran, A.; Bernardi, F.; Garavelli, M.; Gagliardi, L.; Orlandi, G. On the Mechanism of the cis-trans Isomerization in the Lowest Electronic States of Azobenzene: S0, S1, and T1. *J. Am. Chem. Soc.* **2004**, *126*, 3234–3243.
- (214) Bandara, H. M. D.; Burdette, S. C. Photoisomerization in different classes of azobenzene. *Chem. Soc. Rev.* **2011**, *41*, 1809–1825.
- (215) Tan, E. M. M.; Amirjalayer, S.; Smolarek, S.; Vdovin, A.; Zerbetto, F.; Buma, W. J. Fast photodynamics of azobenzene probed by scanning excited-state potential energy surfaces using slow spectroscopy. *Nat. Commun.* **2015**, *6*, 5860.
- (216) Casellas, J.; Bearpark, M. J.; Reguero, M. Excited-State Decay in the Photoisomerisation of Azobenzene: A New Balance between Mechanisms. *ChemPhysChem* **2016**, *17*, 3068–3079.
- (217) Nenov, A.; Borrego-Varillas, R.; Oriana, A.; Ganzer, L.; Segatta, F.; Conti, I.; Segarra-Martí, J.; Omachi, J.; Dapor, M.; Taioli, S. et al. UV-Light-Induced Vibrational Coherences: The Key to Understand Kasha Rule Violation in trans-Azobenzene. *J. Phys. Chem. Lett.* **2018**, *9*, 1534–1541.
- (218) Aleotti, F.; Soprani, L.; Nenov, A.; Bernardi, R.; Arcioni, A.; Zannoni, C.; Garavelli, M. Multidimensional Potential Energy Surfaces Resolved at the RASPT2 Level for Accurate Photoinduced Isomerization Dynamics of Azobenzene. *J. Chem. Theory Comput.* **2019**, *15*, 6813–6823.
- (219) Yu, J. K.; Bannwarth, C.; Liang, R.; Hohenstein, E. G.; Martínez, T. J. Nonadiabatic Dynamics Simulation of the Wavelength-Dependent Photochemistry of Azobenzene Excited to the  $n\pi^*$  and  $\pi\pi^*$  Excited States. *J. Am. Chem. Soc.* **2020**, *142*, 20680–20690.
- (220) Merritt, I. C. D.; Jacquemin, D.; Vacher, M. cis  $\rightarrow$  trans photoisomerisation of azobenzene: a fresh theoretical look. *Phys. Chem. Chem. Phys.* **2021**, *23*, 19155–19165.
- (221) Carlini, L.; Montorsi, F.; Wu, Y.; Bolognesi, P.; Borrego-Varillas, R.;

Casavola, A. R.; Castrovilli, M. C.; Chiarinelli, J.; Mocci, D.; Vismarra, F. et al. Electron and ion spectroscopy of azobenzene in the valence and core shells. *J. Chem. Phys.* **2023**, *158*, 054201.

- (222) Ehlert, C.; Gühr, M.; Saalfrank, P. An efficient first principles method for molecular pump-probe NEXAFS spectra: Application to thymine and azobenzene. *J. Chem. Phys.* **2018**, *149*, 144112.
- (223) Segatta, F.; Nenov, A.; Orlandi, S.; Arcioni, A.; Mukamel, S.; Garavelli, M. Exploring the capabilities of optical pump X-ray probe NEXAFS spectroscopy to track photo-induced dynamics mediated by conical intersections. *Faraday Discuss.* **2019**, *221*, 245–264.
- (224) Wei-Guang Diao, E. A New Trans-to-Cis Photoisomerization Mechanism of Azobenzene on the S1( $n,\pi^*$ ) Surface. *J. Phys. Chem. A* **2004**, *108*, 950–956.
- (225) Ohio Supercomputer Center. 1987; <http://osc.edu/ark:/19495/f5s1ph73>, accessed 2024-05-10.

# TOC Graphic

